

000 001 002 003 004 005 006 007 008 009 010 011 012 013 014 015 016 017 018 019 020 021 022 023 024 025 026 027 028 029 030 031 032 033 034 035 036 037 038 039 040 041 042 043 044 045 046 047 048 049 050 051 052 053 INFERENCE-TIME ALIGNMENT CONTROL FOR DIFFUSION MODELS WITH REINFORCEMENT LEARNING GUIDANCE

Anonymous authors

Paper under double-blind review

ABSTRACT

Denoising-based generative models, particularly diffusion and flow matching algorithms, have achieved remarkable success. However, aligning their output distributions with complex downstream objectives remains challenging. While reinforcement learning (RL) fine-tuning methods, inspired by advances in RL from human feedback (RLHF) for large language models, have been adapted to these generative frameworks, current RL approaches offer limited flexibility in controlling alignment strength after fine-tuning. In this work, we view RL fine-tuning for diffusion models through the lens of stochastic differential equations and implicit reward conditioning. We introduce *Reinforcement Learning Guidance* (RLG), an inference-time method that adapts Classifier-Free Guidance (CFG) by combining the outputs of the base and RL fine-tuned models via a geometric average. Our theoretical analysis shows that RLG’s guidance scale is mathematically equivalent to adjusting the KL-regularization coefficient in standard RL objectives, enabling dynamic control over the alignment-quality trade-off without further training. Extensive experiments demonstrate that RLG consistently improves the performance of RL fine-tuned models across various architectures, RL algorithms, and downstream tasks, including human preferences, compositional control, compressibility, and text rendering. Furthermore, RLG supports both interpolation and extrapolation, thereby offering unprecedented flexibility in controlling generative alignment. Our approach provides a practical and theoretically sound solution for enhancing and controlling diffusion model alignment at inference. The source code for RLG is available in the anonymous repository: ¹.

1 INTRODUCTION

While denoising-based generative models—primarily diffusion Ho et al. (2020); Rombach et al. (2022) and flow matching Lipman et al. (2022); Esser et al. (2024) algorithms—have gained widespread usage, a key challenge is aligning their learned distribution with complex downstream objectives such as human preferences Kirstain et al. (2023), compositional correctness Ghosh et al. (2023), text rendering Liu et al. (2025b), or data compressibility Black et al. (2023). Existing approaches include reward-weighted regression Peng et al.; Lee et al. (2023); Fan et al. (2025), direct reward fine-tuning Xu et al. (2023); Prabhudesai et al. (2023); Clark et al. (2023), and reinforcement learning (RL) fine-tuning.

Owing to significant advancements in Reinforcement Learning from Human Feedback (RLHF) Black et al. (2023); Lee et al. (2023) for Large Language Models (LLMs), RL has been adapted to diffusion models by formulating denoising as a multi-step decision-making process, enabling algorithms like REINFORCE Williams (1992); Mohamed et al. (2020); Black et al. (2023), Direct Preference Optimization (DPO) Rafailov et al. (2023); Wallace et al. (2024), and Group Relative Policy Optimization (GRPO) Shao et al. (2024); Liu et al. (2025b)—to diffusion models. However, current RL methods for diffusion models still exhibit several limitations, primarily in two respects. First, the exact probability of a sampled image is intractable due to the nature of diffusion algorithms, which undermines the effectiveness of existing RL algorithms Black et al. (2023); Gong

¹<https://anonymous.4open.science/r/Reinforcement-learning-guidance-7B5A/>

054
055
056
057
058
059
060
061
062
063
064
065
066
067
068
069
070
071
072
073
074
075

Figure 1: Selected qualitative results for the human preference alignment task using SD3.5-M with GRPO and our RLG. The PickScore is displayed on each image. As the RLG scale increases, the images generally become more detailed, aesthetically pleasing, which is corroborated by the rising PickScores.

et al. (2025). Second, the degree to which the base model aligns with downstream objectives remains fixed after RL fine-tuning and is sensitive to hyperparameter choices, such as the Kullback–Leibler (KL) coefficient. This inflexibility prevents users from dynamically balancing alignment and generation quality, which may be crucial in applications such as compressibility.

In this work, we draw inspiration from the stochastic differential equation (SDE) nature of denoising-based generative models Song et al. (2020b), which motivates us to interpret RL fine-tuning of diffusion models as a special case of generation conditioned on implicit rewards learned through reinforcement learning objectives Rafailov et al. (2024); Zhu et al. (2025); Cui et al. (2025). Building upon this perspective, we introduce an inference-time enhancement technique, *Reinforcement Learning Guidance* (RLG), which adapts the established controlling approach, Classifier-Free Guidance (CFG) Ho & Salimans (2022); Zheng et al. (2023), by computing a weighted geometric average of the outputs from the base model and the RL fine-tuned model. We theoretically demonstrate that this weighted averaging has the same effect as modifying the KL coefficient in RL fine-tuning, but crucially, it requires no additional training.

Empirical results on downstream tasks demonstrate that RLG enhances the performance of RL fine-tuned models across diverse tasks and setups: various model types (diffusion and flow matching), a range of RL methods (policy gradient, DPO, GRPO, etc.), and multiple downstream objectives (image aesthetics, compositional control, compressibility, text rendering, inpainting, and personalized generation). Furthermore, RLG supports both interpolation and extrapolation, thereby offering substantial flexibility in controlling the degree of alignment with downstream objectives.

Our contributions are summarized as follows:

102
103
104
105
106
107

- We propose **Reinforcement Learning Guidance** (RLG), a novel, training-free approach for enhancing and controlling the inference-time alignment of denoising-based generative models.
- We provide a theoretical foundation for RLG, demonstrating that its guidance scale is mathematically equivalent to adjusting the KL-regularization coefficient in the underlying RL objective. This analysis formally accounts for the effectiveness of extrapolation ($w > 1$).

108 • We perform extensive experiments on a diverse set of alignment tasks, showing that RLG
 109 consistently enhances performance by enabling models to surpass their original fine-tuned
 110 capabilities, while also allowing for flexible trade-offs between competing objectives.
 111

112 **2 BACKGROUND**
 113

114 **2.1 DIFFUSION AND FLOW-BASED GENERATIVE MODELS**
 115

116 Diffusion Ho et al. (2020); Song et al. (2020a); Rombach et al. (2022) and flow-based Lipman et al.
 117 (2022); Liu et al. (2022); Esser et al. (2024) models generate data by transforming noise into samples
 118 via either stochastic (SDE) or deterministic (ODE) processes. Diffusion models, e.g., DDPM Ho
 119 et al. (2020), DDIM Song et al. (2020a), and Stable Diffusion Rombach et al. (2022), corrupt data
 120 with noise and train a network to learn the score function $s(\mathbf{X}_t, t)$ for reverse denoising Song et al.
 121 (2020b). Flow-based approaches such as Flow Matching Lipman et al. (2022) learn a velocity field
 122 $\mathbf{v}(\mathbf{X}_t, t)$ to follow a deterministic path from prior to data Liu et al. (2022); Esser et al. (2024); Tong
 123 et al. (2023); Kong et al. (2024); Liu et al. (2025a); Wan et al. (2025).

124 A reference flow $(X_t)_{t \in [0,1]}$ interpolates between $X_1 \sim p_1$ and $X_0 \sim p_{\text{data}}$:

$$125 \quad X_t = \beta_t X_1 + \alpha_t X_0, \quad \alpha_0 = \beta_1 = 0, \quad \alpha_1 = \beta_0 = 1. \quad (1)$$

127 For ODE-based Flow Matching, the model is trained to match the reference velocity:

$$128 \quad \mathbf{v}(\mathbf{X}_t, t) \approx \dot{\beta}_t X_0 + \dot{\alpha}_t X_1.$$

129 Diffusion models solve an SDE with noise schedule $\sigma(t)$, typically parameterized by $\alpha_t = \sqrt{\bar{\alpha}_t}$,
 130 $\beta_t = \sqrt{1 - \bar{\alpha}_t}$.

132 Formally, the velocity field in Flow Matching can be written in terms of the score function as

$$133 \quad \mathbf{v}(\mathbf{x}, t) = \left(\frac{\dot{\alpha}_t}{\alpha_t} \right) \mathbf{x} + \beta_t \left(\frac{\dot{\alpha}_t}{\alpha_t} \beta_t - \dot{\beta}_t \right) \mathbf{s}(\mathbf{x}, t). \quad (2)$$

136 The two paradigms unify under the SDE Song et al. (2020b):

$$137 \quad d\mathbf{X}_t = \left(\mathbf{v}(\mathbf{X}_t, t) - \frac{1}{2} \sigma(t)^2 \mathbf{s}(\mathbf{X}_t, t) \right) dt + \sigma(t) dw, \quad (3)$$

139 where w is Brownian motion; diffusion and Flow Matching differ in \mathbf{v} , \mathbf{s} , and $\sigma(t)$.
 140

141 **2.2 GUIDANCE AND CONTROL IN GENERATIVE MODELS**
 142

143 Controlling generative model outputs is essential for conditional generation tasks. Early work such
 144 as Classifier Guidance (CG) steers the generation process using gradients from a separately trained
 145 classifier Dhariwal & Nichol (2021), but this approach is computationally costly and limited by the
 146 need for an external model.

147 Classifier-Free Guidance (CFG) has become the standard alternative Ho & Salimans (2022). At
 148 inference, CFG computes two passes: one with the actual condition c (e.g., text-guided) and one
 149 with the null condition \emptyset . The guided velocity field $\hat{\mathbf{v}}_\theta$ is a linear interpolation between these two
 150 outputs:

$$151 \quad \hat{\mathbf{v}}_\theta(\mathbf{x}_t, t|c) \triangleq (1 - \omega) \mathbf{v}_\theta(\mathbf{x}_t, t|\emptyset) + \omega \mathbf{v}_\theta(\mathbf{x}_t, t|c), \quad (4)$$

152 where ω is the guidance scale parameter. Setting $\omega = 1$ recovers conditional generation, while
 153 $\omega > 1$ extrapolates beyond the conditional prediction.

154 The same principle applies to the model's score function:

$$155 \quad \hat{\mathbf{s}}_\theta(\mathbf{x}_t, t|c) \triangleq (1 - \omega) \mathbf{s}_\theta(\mathbf{x}_t, t|\emptyset) + \omega \mathbf{s}_\theta(\mathbf{x}_t, t|c), \quad (5)$$

157 where $\mathbf{s}_\theta(\mathbf{x}_t, t|c) = \nabla_{\mathbf{x}_t} \log p_\theta(\mathbf{x}_t|c)$. This can be equivalently written as:

$$158 \quad \hat{\mathbf{s}}_\theta(\mathbf{x}_t, t|c) = \nabla_{\mathbf{x}_t} \log (p_\theta(\mathbf{x}_t)^{1-\omega} p_\theta(\mathbf{x}_t|c)^\omega), \quad (6)$$

160 Although CFG is highly effective, most existing methods focus on adherence to training-time con-
 161 ditions such as text condition, leaving open the possibility of leveraging reinforcement learning
 162 rewards as dynamic, flexible forms of guidance.

162 2.3 PREFERENCE ALIGNMENT IN GENERATIVE MODELS
163164 Preference learning methods from LLMs have been adapted to fine-tune T2I diffusion models for
165 human alignment. A pre-trained model π_{ref} is fine-tuned to maximize a reward $R(\mathbf{x})$ under KL
166 regularization:

167
$$\pi_{\theta}^* = \arg \max_{\pi_{\theta}} \mathbb{E}_{\mathbf{x} \sim \pi_{\theta}} [R(\mathbf{x})] - \beta D_{\text{KL}}(\pi_{\theta} \parallel \pi_{\text{ref}}), \quad (7)$$

168 where β controls the reward-regularization trade-off.
169170 The optimal solution to this problem shows the aligned policy is a re-weighted reference policy, with
171 weights exponentially proportional to the reward Peng et al.; Lee et al. (2023); Fan et al. (2025):

172
$$p^*(\mathbf{x}) \propto p_{\text{ref}}(\mathbf{x}) \exp \left(\frac{1}{\beta} R(\mathbf{x}) \right). \quad (8)$$

173

174 This objective can be optimized with policy gradient methods include PPO Schulman et al. (2017);
175 Black et al. (2023), as well as direct approaches such as DPO Rafailov et al. (2023); Wallace et al.
176 (2024) and GRPO Sun et al. (2025); Shao et al. (2024). However, many alignment methods may
177 overlook characteristics of diffusion models. For instance, Diffusion-DPO Wallace et al. (2024)
178 is upper-bounded by the original DPO loss. In particular, integrating reinforcement learning ob-
179 jectives with diffusion-specific techniques—such as Classifier-Free Guidance (CFG) Ho & Sal-
180 mians (2022)—remains underexplored, presenting opportunities to design approaches that combine
181 reward-based alignment with the generative priors and guidance capabilities unique to diffusion.
182183 **Concurrent Work.** While finalizing our paper, two concurrent works, CFGRL(Frans et al., 2025)
184 and Diffusion Blend(Cheng et al., 2025), appeared. Both investigate inference-time manipulation
185 techniques via score interpolation. However, CFGRL focuses solely on offline RL and simple task
186 settings, while Diffusion Blend does not establish a connection between interpolation and implicit
187 reward guidance. In contrast, RLG offers a comprehensive analysis of score interpolation from the
188 perspective of implicit classifier guidance and demonstrates its effectiveness across various image
189 generation models, RL algorithms, and tasks.
190191 3 METHODS
192193 DERIVING REINFORCEMENT LEARNING GUIDANCE (RLG)
194195 Let r represent the desired attribute, such as a high preference score. Following Bayes' rule, the
196 score function of the conditional distribution $p_{\text{ref}}(\mathbf{x}_t | r)$ can be decomposed as:

197
$$\nabla_{\mathbf{x}_t} \log p_{\text{ref}}(\mathbf{x}_t | r) = \nabla_{\mathbf{x}_t} \log p_{\text{ref}}(\mathbf{x}_t) + \nabla_{\mathbf{x}_t} \log p(r | \mathbf{x}_t). \quad (9)$$

198

199 To relate this to a reward function $R(\mathbf{x}_t)$, following Zhu et al. (2025), we model $p(r | \mathbf{x}_t)$ via an
200 energy-based form:

201
$$p(r | \mathbf{x}_t) = \frac{\exp(R(\mathbf{x}_t))}{Z}, \quad Z = \int \exp(R(\mathbf{x}_t)) d\mathbf{x}_t. \quad (10)$$

202

203 Substituting this into Equation 9 yields the general formula for reward gradient guidance:

204
$$\hat{s}(\mathbf{x}_t, t) = s_{\text{ref}}(\mathbf{x}_t, t) + \eta \nabla_{\mathbf{x}_t} R(\mathbf{x}_t). \quad (11)$$

205

206 Here, η is a guidance scale. Since we lack an explicit, differentiable reward model $R(\mathbf{x}_t)$, we draw
207 from the solution to the KL-regularized RL objective (Equation 8) and from Rafailov et al. (2024);
208 Zhu et al. (2025) to define an implicit, time-dependent reward function $R_t(\mathbf{x}_t)$ that represents the
209 preference learned by π_{θ} throughout the generative process:

210
$$R_t(\mathbf{x}_t) \triangleq \beta \log \frac{p_{\theta,t}(\mathbf{x}_t)}{p_{\text{ref},t}(\mathbf{x}_t)}. \quad (12)$$

211

212 $p_{\theta,t}$ and $p_{\text{ref},t}$ are the marginal probability distributions of the noisy sample \mathbf{x}_t under the RL-aligned
213 and reference models, respectively, and β is the KL-coefficient from the original RL fine-tuning
214 objective.

216 **Algorithm 1** Sampling with Reinforcement Learning Guidance (RLG)

```

217 1: Input: Pre-trained model velocity  $\mathbf{v}_{\text{ref}}$ , RL-finetuned model velocity  $\mathbf{v}_{\text{RL}}$ , condition  $c$ , RLG
218 scale  $w$ , number of steps  $N$ .
219 2: Sample initial noise  $\mathbf{x}_1 \sim \mathcal{N}(0, \mathbf{I})$ .
220 3: for  $t = 1, \dots, N$  do
221 4:   Compute reference velocity:  $\mathbf{v}_{\text{ref},t} = \mathbf{v}_{\text{ref}}(\mathbf{x}_t, t|c)$ .
222 5:   Compute RL-aligned velocity:  $\mathbf{v}_{\text{RL},t} = \mathbf{v}_{\text{RL}}(\mathbf{x}_t, t|c)$ .
223 6:   Compute the guided velocity using RLG:
224 7:    $\hat{\mathbf{v}}_{\text{RLG},t} = (1 - w)\mathbf{v}_{\text{ref},t} + w\mathbf{v}_{\text{RL},t}$ .
225 8:   Update the sample using a chosen ODE solver step:
226 9:    $\mathbf{x}_{t+1} = \text{SolverStep}(\mathbf{x}_t, \hat{\mathbf{v}}_{\text{RLG},t})$ .
227 10: end for
228 11: Return: Generated sample  $\mathbf{x}_{N+1}$ .

```

230 To use this implicit reward for guidance, we take its gradient with respect to \mathbf{x}_t , yielding a simple
231 result:
232

$$\begin{aligned} \nabla_{\mathbf{x}_t} R_t(\mathbf{x}_t) &= \beta [\nabla_{\mathbf{x}_t} \log p_{\theta,t} - \nabla_{\mathbf{x}_t} \log p_{\text{ref},t}] \\ &= \beta [\mathbf{s}_{\theta}(\mathbf{x}_t, t) - \mathbf{s}_{\text{ref}}(\mathbf{x}_t, t)]. \end{aligned} \quad (13)$$

236 Substituting this into Equation 9 yields the general formula for reward gradient guidance:
237

$$\hat{\mathbf{s}}_{\text{RLG}}(\mathbf{x}_t, t) = (1 - w)\mathbf{s}_{\text{ref}} + w\mathbf{s}_{\theta}, \quad (14)$$

239 which is a linear interpolation of score functions, interpretable as implicit reward gradient guidance.
240 Using Eq. 2, the same applies to velocity fields, yielding:
241

$$\hat{\mathbf{v}}_{\text{RLG}}(\mathbf{x}_t, t) = (1 - w)\mathbf{v}_{\text{ref}}(\mathbf{x}_t, t) + w\mathbf{v}_{\theta}(\mathbf{x}_t, t), \quad (15)$$

243 where w is the RLG guidance scale. A value of $w = 0$ recovers the original model, $w = 1$ recovers
244 the RL-finetuned model, and $w > 1$ extrapolates the learned alignment. The full sampling procedure
245 is outlined in Algorithm 1.

246 **THEORETICAL JUSTIFICATION: RLG AS KL-COEFFICIENT CONTROL**
247

248 RLG's mechanisms can be explained by a complementary theoretical justification. Similar to
249 CFG Ho & Salimans (2022), the guided score $\hat{\mathbf{s}}_{\text{RLG}}$ corresponds to sampling from a new time-
250 dependent distribution:
251

$$\hat{\mathbf{s}}_{\text{RLG}} = \nabla_{\mathbf{x}_t} \log (p_{\text{ref},t}(\mathbf{x}_t)^{1-w} p_{\theta,t}(\mathbf{x}_t)^w). \quad (16)$$

253 As $t \rightarrow 0$, the noisy sample \mathbf{x}_t approaches the clean data \mathbf{x}_0 . In this limit, the marginal distributions
254 $p_{\text{ref},t}$ and $p_{\theta,t}$ converge to their corresponding final distributions, $p_{\text{ref}}(\mathbf{x}_0)$ and $p_{\theta}(\mathbf{x}_0)$. Therefore, the
255 score function guiding the final steps of generation points towards a target distribution $\hat{p}_{\text{RLG}}(\mathbf{x}_0)$ of
256 the form: $p_{\text{ref}}(\mathbf{x}_0)^{1-w} p_{\theta}(\mathbf{x}_0)^w$.
257

Assuming the RL-finetuned model π_{θ} has converged to the optimal distribution from Rafailov et al.
(2024; 2023) (i.e., $p_{\theta}(\mathbf{x}_0) \propto p_{\text{ref}}(\mathbf{x}_0) \exp(\frac{1}{\beta} R(\mathbf{x}_0))$), we can substitute this into the expression for
the RLG distribution:
258

$$\begin{aligned} \hat{p}_{\text{RLG}}(\mathbf{x}_0) &\propto p_{\text{ref}}(\mathbf{x}_0)^{1-w} \left(p_{\text{ref}}(\mathbf{x}_0) \exp \left(\frac{1}{\beta} R(\mathbf{x}_0) \right) \right)^w \\ &\propto p_{\text{ref}}(\mathbf{x}_0) \exp \left(\frac{1}{\beta/w} R(\mathbf{x}_0) \right). \end{aligned} \quad (17)$$

265 This derivation reveals a crucial insight: RLG with guidance scale w is mathematically equivalent to
266 sampling from the optimal policy of an RL objective with an effective KL-regularization coefficient
267 of β/w .
268

269 We empirically validated this result with a small-scale demonstration. Our experimental setting uses
a flow matching model defined on the real line, with a pretrained target (base) Gaussian mixture

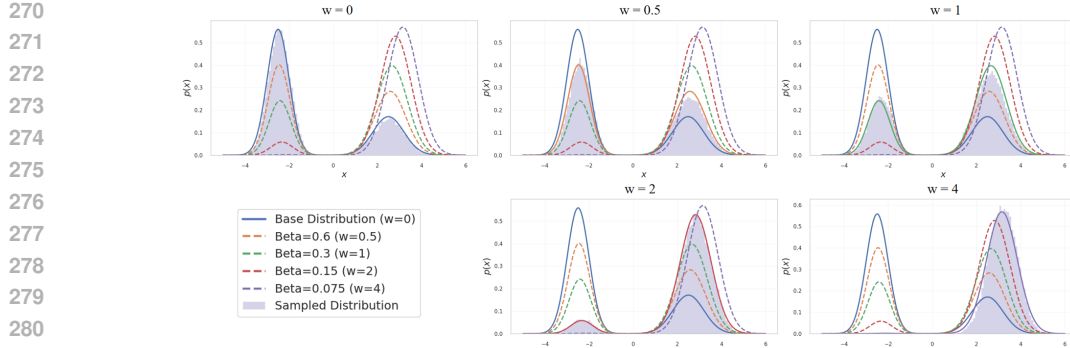


Figure 2: Small-scale demonstration supporting the theoretical justification of RLG. Each subplot shows the sampled distribution under a different RLG weight w , while the curves represent the corresponding theoretically predicted RL-fine-tuned distributions. Here, β denotes the KL regularization coefficient.

distribution: $p_{\text{base}}(x) \triangleq 0.7\mathcal{N}(-2.5, 0.25) + 0.3\mathcal{N}(2.5, 0.49)$. The reward function is $r(x) = 0.1x$. We fine-tuned the pretrained model using a policy gradient algorithm with a KL coefficient $\beta = 0.3$, a batch size of 64, and a learning rate of 1×10^{-5} . Figure 2 presents sampled distributions under various RLG weights w , alongside the corresponding theoretically predicted RL targets. Results show that RLG-sampled distributions closely match theoretically predicted RL targets, corroborating our analysis.

Selecting $w > 1$ dynamically reduces the regularization penalty at inference time, allowing the model to pursue higher rewards more aggressively than the original RL-fine-tuned model. Conversely, $w < 1$ increases regularization. This provides principled justification for RLG’s capacity to extrapolate or interpolate beyond the learned policy, offering a powerful and theoretically grounded mechanism to control the trade-off between alignment and fidelity.

4 EXPERIMENTS

This section empirically validates RLG’s effectiveness. Experiments are conducted on various text-to-image (T2I) alignment tasks. In each case, the original pre-trained model serves as \mathbf{v}_{ref} , and the RL-aligned model as \mathbf{v}_{θ} . RLG is applied as described in Equation 15. For all experiments, sampling steps were set to 20. A comprehensive list of additional hyperparameters can be found in the appendix F.1.

4.1 RLG UNIVERSALLY ENHANCES ALIGNMENT ACROSS DIVERSE TASKS

A key strength of RLG is its broad applicability. This training-free method consistently enhances model capabilities across diverse alignment tasks, from high-level compositional understanding to fine-grained subject fidelity.

Structured Generation: Compositionality and Text Rendering. RLG is first evaluated on tasks requiring precise adherence to structured prompts. For compositional generation, the GenEval benchmark Ghosh et al. (2023) is used with a GRPO-finetuned SD3.5-M model Liu et al. (2025b). This task tests the model’s ability to correctly render object relationships, counts, and attributes. Following the benchmark’s protocol, a Mask2Former model Cheng et al. (2022) verifies the presence and properties of objects specified in prompts within the official GenEval test set.

For visual text rendering, an GRPO-finetuned SD3.5-M model on the Optical Character Recognition (OCR) task Mori et al. (1999) (also from Liu et al. (2025b)) measures its ability to accurately render text from prompts that contain the exact string to appear in the image. OCR accuracy is calculated based on the normalized edit distance ($1 - d_{\text{norm}}$), where d_{norm} is the Levenshtein distance Yujian &

324
 325 Table 1: Quantitative results for Human Preference Alignment. Mean scores for Aesthetic Score,
 326 ImageReward, and PickScore are reported. For each metric, values after the slash (/) indicate win
 327 rates (%) against the standard RL-finetuned model ($w_{RL} = 1.0$). SD denotes stable-diffusion mod-
 328 els Rombach et al. (2022).

Model	RL	w_{RL}	Aesthetic Score (\uparrow)	ImageReward (\uparrow)	PickScore (\uparrow)
SD1.5	DPO Lee et al. (2023)	0.0	5.51 / 38.48%	-0.02 / 36.67%	20.03 / 27.34%
		1.0	5.61	0.20	20.39
		1.4	5.63 / 53.56%	0.25 / 53.47%	20.46 / 57.86%
		2.4	5.64 / 56.25%	0.32 / 57.08%	20.56 / 61.23%
SDXL-base	SPO Liang et al. (2024)	0.0	6.10 / 17.87%	0.72 / 18.02%	21.66 / 7.62%
		1.0	6.42	1.12	22.69
		1.2	6.45 / 59.81%	1.13 / 54.10%	22.71 / 54.64%
		1.4	6.48 / 62.99%	1.14 / 54.15%	22.71 / 54.35%
SD3.5-M	GRPO Liu et al. (2025b)	0.0	5.97 / 11.33%	0.99 / 17.29%	21.75 / 2.39%
		1.0	6.45	1.40	23.29
		1.4	6.54 / 69.28%	1.40 / 54.44%	23.48 / 74.95%
		2.2	6.64 / 77.39%	1.39 / 53.56%	23.58 / 73.68%

341
 342 Table 2: Ppervformance on the GenEval benchmark. We report accuracy (%) for each compositional
 343 sub-task and the overall average score across different RLG guidance scales (w_{RL}).
 344

Model	w_{RL}	Single Obj.	Two Obj.	Colors	Color Attr.	Counting	Position	Overall Score
SD3.5-M	0.0	97.81	80.56	80.05	51.75	53.44	23.00	64.44
	1.0	100.00	98.99	89.63	84.00	92.81	93.75	93.20
	1.2	99.69	98.74	90.69	86.11	92.81	94.25	93.72
	1.4	99.69	99.24	91.49	86.50	94.69	94.50	94.35
	1.6	100.00	98.99	91.76	86.00	93.75	95.00	94.25

351
 352 Bo (2007) between generated text (extracted using PaddleOCR Authors (2020)) and the ground-truth
 353 text, normalized by ground-truth text length.
 354

355 Tables 2, 3 and Figures 11, 8 show that while RL-finetuned models ($w_{RL} = 1.0$) already substantially
 356 improve over their base counterparts, extrapolating with RLG unlocks further significant gains. On
 357 GenEval, RLG pushes the overall score from 93.20% to a peak of **94.35%**, improving almost all key
 358 compositional tasks. On the OCR task, RLG boosts accuracy from 88.6% to a new state-of-the-art
 359 of **93.0%** with minimal impact on aesthetic score. These results confirm RLG effectively amplifies
 360 the model’s learned ability to follow complex structural constraints.
 361

362 Table 3: Quantitative results for the visual text rendering task. This table shows the Optical Character
 363 Recognition (OCR) accuracy at different RLG guidance scales.
 364

Model	w_{RL}	OCR Acc (\uparrow)	Aesthetic Score (\uparrow)
SD3.5-M	0.0	0.543	5.40
	0.4	0.785	5.28
	0.6	0.838	5.25
	1.0	0.886	5.20
	1.2	0.894	5.17
	1.6	0.910	5.13
	2.2	0.921	5.07
	2.8	0.930	5.00

375 **Fidelity-Driven Generation: Inpainting and Personalization.** We next test RLG on tasks de-
 376 manding high fidelity to reference content: image inpainting and personalized generation. For im-
 377 age inpainting, we use the PrefPaint Bui et al. (2025) model, an RL-finetuned model built on stable-
 378 diffusion-inpainting Podell et al. (2023) and designed to fill masked regions according to human

378 preferences. To evaluate quality, we use Preference Reward metrics Bui et al. (2025) on the dataset
 379 detailed in appendix I. For personalized generation, we use PatchDPO Huang et al. (2025), an RL-
 380 finetuned model optimized to maintain subject identity from reference images. Here, the original
 381 pre-trained model (IP-Adapter-Plus Ye et al. (2023)) serves as the base (\mathbf{v}_{ref}), and PatchDPO as the
 382 RL-aligned model (\mathbf{v}_{θ}). Subject fidelity is measured using two standard image-similarity metrics:
 383 CLIP-I Ruiz et al. (2023) and DINO Caron et al. (2021), evaluated on the DreamBench Ruiz et al.
 384 (2023) benchmark, detailed in appendix J.

385 The results, summarized in Table 4, again show RLG’s effectiveness. For inpainting, RLG pushes
 386 the preference score beyond the original PrefPaint model, peaking at **0.368**. For personalized gen-
 387 eration, RLG further refines subject fidelity, increasing the DINO score to **0.730** and CLIP-I score
 388 to **0.843**. In both cases, RLG provides measurable enhancement over state-of-the-art RL-finetuned
 389 models without any additional training.

390
 391 Table 4: RLG enhances performance on distinct fidelity-driven tasks. The evaluation metrics are
 392 presented separately for each task.

<i>Task: Image Inpainting</i>		<i>Task: Personalized Generation</i>		
Method	Pref. Reward (↑)	Method	DINO (↑)	CLIP-I (↑)
Base ($w_{\text{RL}} = 0$)	0.080	IP-Adapter-Plus ($w_{\text{RL}} = 0$)	0.692	0.826
PrefPaint ($w_{\text{RL}} = 1.0$)	0.358	PatchDPO ($w_{\text{RL}} = 1.0$)	0.724	0.839
RLG ($w_{\text{RL}} = 1.2$)	0.367	RLG ($w = 1.2$)	0.730	0.841
RLG ($w_{\text{RL}} = 1.4$)	0.368	RLG ($w = 1.8$)	0.730	0.843
RLG ($w_{\text{RL}} = 1.6$)	0.366			

4.2 RLG IS EFFECTIVE ACROSS DIVERSE RL ALGORITHMS AND MODEL ARCHITECTURES

401
 402 To demonstrate RLG’s broad applicability and model-agnostic nature, we evaluate its consistent
 403 enhancement of models differing in generative architecture (i.e., standard diffusion vs. modern flow
 404 matching) and the specific reinforcement learning algorithm used for their initial alignment. This
 405 also extends to algorithms such as GRPO, whose optimal policy does not necessarily conform to
 406 Equation 8.

407
 408 **Experimental Setup.** We analyze RLG on the human preference alignment task, leveraging three
 409 distinct, publicly available RL-finetuned models, each representing a unique combination of archi-
 410 tecture and alignment method:

- 411 • **SD1.5 + DPO:** A Stable Diffusion v1.5 model Rombach et al. (2022) aligned using Direct
 412 Preference Optimization (DPO) Wallace et al. (2024).
- 413 • **SDXL + SPO:** A Stable Diffusion XL model Podell et al. (2023) aligned using Step-wise
 414 Preference Optimization (SPO) Liang et al. (2024).
- 415 • **SD3.5-M + GRPO:** A Stable Diffusion 3.5 Medium flow matching model Esser et al.
 416 (2024) aligned using Group Relative Policy Optimization (GRPO) Liu et al. (2025b).

417
 418 For evaluation, we use three established automated reward models: Aesthetic Score, ImageReward,
 419 and PickScore, with details provided in the appendix.

420
 421 **Results.** Table 1 summarizes quantitative results, unequivocally demonstrating that RLG con-
 422 sistently delivers a significant performance boost across all configurations. The effect is particu-
 423 larly pronounced on the state-of-the-art GRPO-tuned SD3.5-M flow model, where RLG achieves
 424 a **74.95%** win rate on PickScore against the original finetuned model ($w_{\text{RL}} = 1.0$). As visually
 425 confirmed in Figures 1, 5, 6 and 7, increasing the RLG scale consistently enhances image detail and
 426 aesthetic appeal.

4.3 RLG ENABLES FLEXIBLE CONTROL OVER ALIGNMENT STRENGTH

427
 428 Standard RL fine-tuning fixes alignment strength, offering no inference-time flexibility. In contrast,
 429 RLG dynamically controls alignment strength with a powerful, training-free mechanism.

432
 433 Table 5: RLG provides dynamic control over image compressibility. RLG allows for both interpo-
 434 lation and extrapolation beyond the original RL-tuned model’s capability ($w_{RL} = 1.0$).

Task	w_{RL}	Compression Ratio
Low Compressibility	0.4	1.14
	0.6	1.22
	1.0	1.35
	1.6	1.43
	3.0	1.37
High Compressibility	0.4	0.75
	0.6	0.64
	1.0	0.45
	1.6	0.18
	2.2	0.17

445
 446
 447 **Controlling a Fundamental Property: Image Compressibility.** We first demonstrate RLG’s
 448 control over image compressibility, a low-level property. We used two DDPO-finetuned SD1.4
 449 models Black et al. (2023) to reward either high or low image compressibility. Standard RL pro-
 450 duces a model with fixed alignment; for instance, the low-compressibility model is locked at a 1.35
 451 compression ratio in average (where $w_{RL} = 1.0$). RLG transforms this static point into a dynamic
 452 spectrum. As shown in Table 5, users can weaken alignment by setting $w_{RL} < 1.0$ (e.g., achieving
 453 a 1.14 ratio) or intensify it with $w_{RL} > 1.0$, pushing the ratio beyond the fine-tuned limit to a peak
 454 of **1.43**. RLG thus provides an inference-time ‘slider’ for alignment strength, a capability static
 455 fine-tuning lacks.

456
 457 **Balancing Competing Objectives: Text Accuracy vs. Aesthetics.** Maximizing one alignment
 458 objective often compromises another. Table 3 illustrates this conflict. The standard RL-finetuned
 459 model ($w_{RL} = 1.0$) achieves 88.6% OCR accuracy, but its Aesthetic Score is fixed at 5.20. This
 460 trade-off is unalterable. RLG transforms this static outcome into flexible control. For instance, users
 461 prioritizing aesthetics over maximum text accuracy can set $w_{RL} < 1.0$. Conversely, others can push
 462 for peak accuracy at the cost of aesthetics by setting $w_{RL} = 2.8$. This inference-time flexibility for
 463 users to choose their preferred sweet spot on the trade-off curve is a key advantage RLG holds over
 464 static fine-tuning.

465 5 CONCLUSION AND DISCUSSION

466
 467 In this paper, we proposed Reinforcement Learning Guidance (RLG), a training-free method for
 468 dynamically controlling generative model alignment at inference. By interpolating or extrapolat-
 469 ing beyond trained preferences, RLG effectively modulates the KL-regularization penalty to pursue
 470 higher rewards. Extensive experiments show consistent gains across diverse tasks, making RLG a
 471 simple yet powerful control layer over learned preferences.

472
 473 Despite its broad empirical success, RLG has limitations that motivate future work. First, inher-
 474 iting from CFG, RLG shares its fundamental drawback: CFG-based sampling does not guarantee
 475 approximation to the target marginal distribution (Bradley & Nakkiran, 2024; Skreta et al., 2025).
 476 Thus it exhibits inherent flaws in the subsequent analytical derivations. Second, our theory linking
 477 the RLG scale w to the KL coefficient β assumes convergence to the optimal policy under a stand-
 478 ard reward–KL objective. This is an idealized assumption and only holds when the optimization
 479 objective is a standard mixture of expected return and KL divergence. For methods such as GRPO,
 480 the optimal policy does not adhere to this theoretical form (Vojnovic & Yun, 2025). Finally, future
 481 work could explore adaptive RLG scales that vary across timesteps or combine RLG with other
 482 orthogonal control methods to achieve even more nuanced generation.

483 6 REPRODUCIBILITY STATEMENT

484
 485 To ensure reproducibility, we provide the complete implementation of RLG
 in an anonymous repository at <https://anonymous.4open.science/r/>

486 Reinforcement-learning-guidance-7B5A/. The sources of all baseline models
 487 and benchmark datasets are detailed in their respective subsections within Section 4. For reference,
 488 Table 6 consolidates the information and sources of all models utilized in this study.
 489

490 REFERENCES
 491

492 PaddlePaddle Authors. Paddleocr, awesome multilingual ocr toolkits based on paddlepaddle.
 493 <https://github.com/PaddlePaddle/PaddleOCR>, 2020.

494 Kevin Black, Michael Janner, Yilun Du, Ilya Kostrikov, and Sergey Levine. Training diffusion
 495 models with reinforcement learning. *arXiv preprint arXiv:2305.13301*, 2023.

496 Arwen Bradley and Preetum Nakkiran. Classifier-free guidance is a predictor-corrector. *arXiv
 497 preprint arXiv:2408.09000*, 2024.

498 Duy-Bao Bui, Hoang-Khang Nguyen, and Trung-Nghia Le. Prefpaint: Enhancing image inpainting
 499 through expert human feedback, 2025. URL <https://arxiv.org/abs/2506.21834>.

500 Mathilde Caron, Hugo Touvron, Ishan Misra, Hervé Jégou, Julien Mairal, Piotr Bojanowski, and
 501 Armand Joulin. Emerging properties in self-supervised vision transformers. In *Proceedings of
 502 the IEEE/CVF international conference on computer vision*, pp. 9650–9660, 2021.

503 Bowen Cheng, Ishan Misra, Alexander G. Schwing, Alexander Kirillov, and Rohit Girdhar. Masked-
 504 attention mask transformer for universal image segmentation, 2022. URL <https://arxiv.org/abs/2112.01527>.

505 Min Cheng, Fatemeh Doudi, Dileep Kalathil, Mohammad Ghavamzadeh, and Panganamala R Ku-
 506 mar. Diffusion blend: Inference-time multi-preference alignment for diffusion models. *arXiv
 507 preprint arXiv:2505.18547*, 2025.

508 Kevin Clark, Paul Vicol, Kevin Swersky, and David J Fleet. Directly fine-tuning diffusion models
 509 on differentiable rewards. *arXiv preprint arXiv:2309.17400*, 2023.

510 Ganqu Cui, Lifan Yuan, Zefan Wang, Hanbin Wang, Wendi Li, Bingxiang He, Yuchen Fan, Tianyu
 511 Yu, Qixin Xu, Weize Chen, et al. Process reinforcement through implicit rewards. *arXiv preprint
 512 arXiv:2502.01456*, 2025.

513 Prafulla Dhariwal and Alexander Nichol. Diffusion models beat gans on image synthesis. *Advances
 514 in neural information processing systems*, 34:8780–8794, 2021.

515 Patrick Esser, Sumith Kulal, Andreas Blattmann, Rahim Entezari, Jonas Müller, Harry Saini, Yam
 516 Levi, Dominik Lorenz, Axel Sauer, Frederic Boesel, Dustin Podell, Tim Dockhorn, Zion En-
 517 glish, Kyle Lacey, Alex Goodwin, Yannik Marek, and Robin Rombach. Scaling rectified flow
 518 transformers for high-resolution image synthesis, 2024. URL <https://arxiv.org/abs/2403.03206>.

519 Jiajun Fan, Shuaike Shen, Chaoran Cheng, Yuxin Chen, Chumeng Liang, and Ge Liu. On-
 520 line reward-weighted fine-tuning of flow matching with wasserstein regularization, 2025. URL
 521 <https://arxiv.org/abs/2502.06061>.

522 Kevin Frans, Seohong Park, Pieter Abbeel, and Sergey Levine. Diffusion guidance is a controllable
 523 policy improvement operator. *arXiv preprint arXiv:2505.23458*, 2025.

524 Dhruba Ghosh, Hannaneh Hajishirzi, and Ludwig Schmidt. Geneval: An object-focused framework
 525 for evaluating text-to-image alignment. *Advances in Neural Information Processing Systems*, 36:
 526 52132–52152, 2023.

527 Shansan Gong, Ruixiang Zhang, Huangjie Zheng, Jiatao Gu, Navdeep Jaitly, Lingpeng Kong, and
 528 Yizhe Zhang. Diffucoder: Understanding and improving masked diffusion models for code gen-
 529 eration. *arXiv preprint arXiv:2506.20639*, 2025.

530 Jonathan Ho and Tim Salimans. Classifier-free diffusion guidance. *arXiv preprint
 531 arXiv:2207.12598*, 2022.

540 Jonathan Ho, Ajay Jain, and Pieter Abbeel. Denoising diffusion probabilistic models. *Advances in*
 541 *neural information processing systems*, 33:6840–6851, 2020.

542

543 Qihan Huang, Long Chan, Jinlong Liu, Wanggui He, Hao Jiang, Mingli Song, and Jie Song.
 544 Patchdpo: Patch-level dpo for finetuning-free personalized image generation. In *Proceedings*
 545 *of the Computer Vision and Pattern Recognition Conference*, pp. 18369–18378, 2025.

546 Yuval Kirstain, Adam Polyak, Uriel Singer, Shahbuland Matiana, Joe Penna, and Omer Levy. Pick-
 547 a-pic: An open dataset of user preferences for text-to-image generation, 2023. URL <https://arxiv.org/abs/2305.01569>.

548

549 Weijie Kong, Qi Tian, Zijian Zhang, Rox Min, Zuozhuo Dai, Jin Zhou, Jiangfeng Xiong, Xin Li,
 550 Bo Wu, Jianwei Zhang, et al. Hunyuanyvideo: A systematic framework for large video generative
 551 models. *arXiv preprint arXiv:2412.03603*, 2024.

552

553 Kimin Lee, Hao Liu, Moonkyung Ryu, Olivia Watkins, Yuqing Du, Craig Boutilier, Pieter Abbeel,
 554 Mohammad Ghavamzadeh, and Shixiang Shane Gu. Aligning text-to-image models using human
 555 feedback. *arXiv preprint arXiv:2302.12192*, 2023.

556

557 Junnan Li, Dongxu Li, Silvio Savarese, and Steven Hoi. Blip-2: Bootstrapping language-image pre-
 558 training with frozen image encoders and large language models, 2023. URL <https://arxiv.org/abs/2301.12597>.

559

560 Zhanhao Liang, Yuhui Yuan, Shuyang Gu, Bohan Chen, Tiansheng Hang, Mingxi Cheng, Ji Li, and
 561 Liang Zheng. Aesthetic post-training diffusion models from generic preferences with step-by-step
 562 preference optimization. *arXiv preprint arXiv:2406.04314*, 2024.

563

564 Yaron Lipman, Ricky TQ Chen, Heli Ben-Hamu, Maximilian Nickel, and Matt Le. Flow matching
 565 for generative modeling. *arXiv preprint arXiv:2210.02747*, 2022.

566

567 Dongyang Liu, Shicheng Li, Yutong Liu, Zhen Li, Kai Wang, Xinyue Li, Qi Qin, Yufei Liu, Yi Xin,
 568 Zhongyu Li, et al. Lumina-video: Efficient and flexible video generation with multi-scale next-dit.
 569 *arXiv preprint arXiv:2502.06782*, 2025a.

570

571 Jie Liu, Gongye Liu, Jiajun Liang, Yangguang Li, Jiaheng Liu, Xintao Wang, Pengfei Wan,
 572 Di Zhang, and Wanli Ouyang. Flow-grpo: Training flow matching models via online rl. *arXiv*
 573 *preprint arXiv:2505.05470*, 2025b.

574

575 Xingchao Liu, Chengyue Gong, and Qiang Liu. Flow straight and fast: Learning to generate and
 576 transfer data with rectified flow. *arXiv preprint arXiv:2209.03003*, 2022.

577

578 Ze Liu, Yutong Lin, Yue Cao, Han Hu, Yixuan Wei, Zheng Zhang, Stephen Lin, and Baining Guo.
 579 Swin transformer: Hierarchical vision transformer using shifted windows. In *Proceedings of the*
 580 *IEEE/CVF international conference on computer vision*, pp. 10012–10022, 2021.

581

582 Shakir Mohamed, Mihaela Rosca, Michael Figurnov, and Andriy Mnih. Monte carlo gradient esti-
 583 mation in machine learning. *Journal of Machine Learning Research*, 21(132):1–62, 2020.

584

585 Shunji Mori, Hirobumi Nishida, and Hiromitsu Yamada. *Optical character recognition*. John Wiley
 586 & Sons, Inc., 1999.

587

588 XB Peng, A Kumar, G Zhang, S Levine, and Advantage-Weighted Regression. Simple and scalable
 589 off-policy reinforcement learning. *arXiv preprint arXiv:1910.00177*.

590

591 Dustin Podell, Zion English, Kyle Lacey, Andreas Blattmann, Tim Dockhorn, Jonas Müller, Joe
 592 Penna, and Robin Rombach. Sdxl: Improving latent diffusion models for high-resolution image
 593 synthesis, 2023. URL <https://arxiv.org/abs/2307.01952>.

594

595 Mihir Prabhudesai, Anirudh Goyal, Deepak Pathak, and Katerina Fragkiadaki. Aligning text-to-
 596 image diffusion models with reward backpropagation. 2023.

597

598 Alec Radford, Jong Wook Kim, Chris Hallacy, Aditya Ramesh, Gabriel Goh, Sandhini Agar-
 599 wal, Girish Sastry, Amanda Askell, Pamela Mishkin, Jack Clark, Gretchen Krueger, and Ilya
 600 Sutskever. Learning transferable visual models from natural language supervision, 2021. URL
 601 <https://arxiv.org/abs/2103.00020>.

594 Rafael Rafailov, Archit Sharma, Eric Mitchell, Christopher D Manning, Stefano Ermon, and Chelsea
 595 Finn. Direct preference optimization: Your language model is secretly a reward model. *Advances*
 596 *in Neural Information Processing Systems*, 36:53728–53741, 2023.

597

598 Rafael Rafailov, Joey Hejna, Ryan Park, and Chelsea Finn. From r to q^* : Your language model is
 599 secretly a q -function, 2024. URL <https://arxiv.org/abs/2404.12358>.

600 Robin Rombach, Andreas Blattmann, Dominik Lorenz, Patrick Esser, and Björn Ommer. High-
 601 resolution image synthesis with latent diffusion models. In *Proceedings of the IEEE/CVF confer-
 602 ence on computer vision and pattern recognition*, pp. 10684–10695, 2022.

603

604 Nataniel Ruiz, Yuanzhen Li, Varun Jampani, Yael Pritch, Michael Rubinstein, and Kfir Aberman.
 605 Dreambooth: Fine tuning text-to-image diffusion models for subject-driven generation. In *Pro-
 606 ceedings of the IEEE/CVF conference on computer vision and pattern recognition*, pp. 22500–
 607 22510, 2023.

608

609 Christoph Schuhmann and Romain Beaumont. Aesthetic-predictor: A linear estimator on top
 610 of clip to predict the aesthetic quality of pictures. [https://github.com/LAION-AI/
 611 aesthetic-predictor](https://github.com/LAION-AI/aesthetic-predictor), June 2021.

612 John Schulman, Filip Wolski, Prafulla Dhariwal, Alec Radford, and Oleg Klimov. Proximal policy
 613 optimization algorithms. *arXiv preprint arXiv:1707.06347*, 2017.

614

615 Zhihong Shao, Peiyi Wang, Qihao Zhu, Runxin Xu, Junxiao Song, Xiao Bi, Haowei Zhang,
 616 Mingchuan Zhang, YK Li, Y Wu, et al. Deepseekmath: Pushing the limits of mathematical
 617 reasoning in open language models. *arXiv preprint arXiv:2402.03300*, 2024.

618

619 Marta Skreta, Tara Akhoud-Sadegh, Viktor Ohanesian, Roberto Bondesan, Alán Aspuru-Guzik,
 620 Arnaud Doucet, Rob Brekelmans, Alexander Tong, and Kirill Neklyudov. Feynman-kac correc-
 621 tors in diffusion: Annealing, guidance, and product of experts. *arXiv preprint arXiv:2503.02819*,
 622 2025.

623

624 Jiaming Song, Chenlin Meng, and Stefano Ermon. Denoising diffusion implicit models. *arXiv
 625 preprint arXiv:2010.02502*, 2020a.

626

627 Yang Song, Jascha Sohl-Dickstein, Diederik P Kingma, Abhishek Kumar, Stefano Ermon, and Ben
 628 Poole. Score-based generative modeling through stochastic differential equations. *arXiv preprint
 629 arXiv:2011.13456*, 2020b.

630

631 Xiaohui Sun, Ruitong Xiao, Jianye Mo, Bowen Wu, Qun Yu, and Baoxun Wang. F5r-tts: Improv-
 632 ing flow-matching based text-to-speech with group relative policy optimization. *arXiv preprint
 633 arXiv:2504.02407*, 2025.

634

635 Alexander Tong, Kilian Fatras, Nikolay Malkin, Guillaume Huguet, Yanlei Zhang, Jarrid Rector-
 636 Brooks, Guy Wolf, and Yoshua Bengio. Improving and generalizing flow-based generative models
 637 with minibatch optimal transport. *arXiv preprint arXiv:2302.00482*, 2023.

638

639 Milan Vojnovic and Se-Young Yun. What is the alignment objective of grpo? *arXiv preprint
 640 arXiv:2502.18548*, 2025.

641

642 Bram Wallace, Meihua Dang, Rafael Rafailov, Linqi Zhou, Aaron Lou, Senthil Purushwalkam,
 643 Stefano Ermon, Caiming Xiong, Shafiq Joty, and Nikhil Naik. Diffusion model alignment using
 644 direct preference optimization. In *Proceedings of the IEEE/CVF Conference on Computer Vision
 645 and Pattern Recognition*, pp. 8228–8238, 2024.

646

647 Team Wan, Ang Wang, Baole Ai, Bin Wen, Chaojie Mao, Chen-Wei Xie, Di Chen, Feiwu Yu,
 648 Haiming Zhao, Jianxiao Yang, et al. Wan: Open and advanced large-scale video generative
 649 models. *arXiv preprint arXiv:2503.20314*, 2025.

650

651 Ronald J Williams. Simple statistical gradient-following algorithms for connectionist reinforcement
 652 learning. *Machine learning*, 8(3):229–256, 1992.

648 Jiazheng Xu, Xiao Liu, Yuchen Wu, Yuxuan Tong, Qinkai Li, Ming Ding, Jie Tang, and Yuxiao
 649 Dong. Imagereward: Learning and evaluating human preferences for text-to-image generation.
 650 *Advances in Neural Information Processing Systems*, 36:15903–15935, 2023.

651
 652 Hu Ye, Jun Zhang, Sibo Liu, Xiao Han, and Wei Yang. Ip-adapter: Text compatible image prompt
 653 adapter for text-to-image diffusion models. *arXiv preprint arXiv:2308.06721*, 2023.

654 Li Yujian and Liu Bo. A normalized levenshtein distance metric. *IEEE transactions on pattern
 655 analysis and machine intelligence*, 29(6):1091–1095, 2007.

656
 657 QinQing Zheng, Matt Le, Neta Shaul, Yaron Lipman, Aditya Grover, and Ricky TQ Chen. Guided
 658 flows for generative modeling and decision making. *arXiv preprint arXiv:2311.13443*, 2023.

659 Huaisheng Zhu, Teng Xiao, and Vasant G Honavar. Dspo: Direct score preference optimization for
 660 diffusion model alignment. In *The Thirteenth International Conference on Learning Representa-
 661 tions*, 2025.

663 A THE USE OF LARGE LANGUAGE MODELS (LLMs)

664 Large Language Models were used solely for language polishing and writing refinement of this
 665 manuscript, including grammar correction and clarity improvement. All research content, method-
 666 ology, analysis, and conclusions are entirely the original work of the authors.

667 B MODEL SPECIFICATION

668 The following table 6 lists the base model, the RL-finetuned model, the reward models and their
 669 corresponding links.

670 C THEORETICAL DERIVATIONS

671 This appendix provides the formal derivations discussed in the main paper.

672 C.1 PROOF OF THE OPTIMAL POLICY FOR KL-REGULARIZED RL

673 We aim to find the policy π^* that solves the optimization problem defined in Equation 7:

$$674 \pi^* = \arg \max_{\pi} (\mathbb{E}_{\mathbf{x} \sim \pi(\mathbf{x})}[R(\mathbf{x})] - \beta D_{\text{KL}}(\pi(\mathbf{x}) \parallel \pi_{\text{ref}}(\mathbf{x}))) \quad (18)$$

675 subject to the constraint that $\pi(\mathbf{x})$ is a valid probability distribution, i.e., $\int \pi(\mathbf{x}) d\mathbf{x} = 1$.

676 First, we expand the objective functional $J(\pi)$:

$$677 \begin{aligned} 678 J(\pi) &= \int \pi(\mathbf{x}) R(\mathbf{x}) d\mathbf{x} - \beta \int \pi(\mathbf{x}) \log \frac{\pi(\mathbf{x})}{\pi_{\text{ref}}(\mathbf{x})} d\mathbf{x} \\ 679 &= \int (\pi(\mathbf{x}) R(\mathbf{x}) - \beta \pi(\mathbf{x}) \log \pi(\mathbf{x}) + \beta \pi(\mathbf{x}) \log \pi_{\text{ref}}(\mathbf{x})) d\mathbf{x} \end{aligned} \quad (19)$$

680 This is a constrained optimization problem that can be solved using the calculus of variations with a
 681 Lagrange multiplier, λ , for the probability distribution constraint. The Lagrangian is:

$$682 \mathcal{L}(\pi, \lambda) = J(\pi) + \lambda \left(\int \pi(\mathbf{x}) d\mathbf{x} - 1 \right) \quad (20)$$

683 To find the optimal policy π^* , we take the functional derivative of \mathcal{L} with respect to $\pi(\mathbf{x})$ and set it
 684 to zero.

$$685 \begin{aligned} 686 \frac{\delta \mathcal{L}}{\delta \pi(\mathbf{x})} &= \frac{\partial}{\partial \pi(\mathbf{x})} [\pi R - \beta \pi \log \pi + \beta \pi \log \pi_{\text{ref}} + \lambda \pi] = 0 \\ 687 &= R(\mathbf{x}) - \beta(\log \pi(\mathbf{x}) + 1) + \beta \log \pi_{\text{ref}}(\mathbf{x}) + \lambda = 0 \end{aligned} \quad (21)$$

702
703
704
705
706

707 Table 6: Models and Their Corresponding Links.

708 Model/Reward Function	709 Link
710 SD3.5-M Esser et al. (2024)	https://huggingface.co/stabilityai/stable-diffusion-3.5-medium
711 SD1.5 Rombach et al. (2022)	https://huggingface.co/stable-diffusion-v1-5/stable-diffusion-v1-5
712 SD1.4 Rombach et al. (2022)	https://huggingface.co/CompVis/stable-diffusion-v1-4
713 SDXL-base Podell et al. (2023)	https://huggingface.co/stabilityai/stable-diffusion-xl-base-1.0
714 SD3.5M-FlowGRPO-PickScore Liu et al. (2025b)	https://huggingface.co/jieliu/SD3.5M-FlowGRPO-PickScore
715 SD3.5M-FlowGRPO-Text Liu et al. (2025b)	https://huggingface.co/jieliu/SD3.5M-FlowGRPO-Text
716 SD3.5M-FlowGRPO-GenEval Liu et al. (2025b)	https://huggingface.co/jieliu/SD3.5M-FlowGRPO-GenEval
717 dpo-sd1.5-text2image-v1 Lee et al. (2023)	https://huggingface.co/mhdang/dpo-sd1.5-text2image-v1
718 SPO-SDXL-4k-p-10ep Liang et al. (2024)	https://huggingface.co/SPO-Diffusion-Models/SPO-SDXL_4k_p_10ep
719 dpo-sdxl-text2image-v1 Lee et al. (2023)	https://huggingface.co/mhdang/dpo-sdxl-text2image-v1
720 ddpo-compressibility Black et al. (2023)	https://huggingface.co/kvablock/ddpo-compressibility
721 ddpo-incompressibility Black et al. (2023)	https://huggingface.co/kvablock/ddpo-incompressibility
722 Aesthetic Score Schuhmann & Beaumont (2021)	https://github.com/LAION-AI/aesthetic-predictor
723 ImageReward Xu et al. (2023)	https://huggingface.co/THUDM/ImageReward
724 PickScore Kirstain et al. (2023)	https://huggingface.co/yuvalkirstain/PickScore_v1
725 clip-vit-large-patch14 Radford et al. (2021)	https://huggingface.co/openai/clip-vit-large-patch14
726 stable-diffusion-inpainting Podell et al. (2023)	https://aihub.caict.ac.cn/models/runwayml/stable-diffusion-inpainting
727 prepaint Bui et al. (2025)	https://huggingface.co/kd5678/paint-v1.0
728 prepaintreward Bui et al. (2025)	https://huggingface.co/kd5678/paintReward
729 IP-Adapter-Plus Ye et al. (2023)	https://huggingface.co/h94/IP-Adapter
730 PatchDPO Huang et al. (2025)	https://huggingface.co/hqhQAQ/PatchDPO

751
752
753
754
755

756 Now, we solve for $\log \pi(\mathbf{x})$:

$$\begin{aligned} 758 \quad \beta \log \pi(\mathbf{x}) &= R(\mathbf{x}) + \beta \log \pi_{\text{ref}}(\mathbf{x}) + \lambda - \beta \\ 759 \quad \log \pi(\mathbf{x}) &= \frac{1}{\beta} R(\mathbf{x}) + \log \pi_{\text{ref}}(\mathbf{x}) + \frac{\lambda - \beta}{\beta} \end{aligned} \quad (22)$$

761 Exponentiating both sides gives the form of the optimal policy $\pi^*(\mathbf{x})$:

$$\begin{aligned} 763 \quad \pi^*(\mathbf{x}) &= \exp \left(\frac{1}{\beta} R(\mathbf{x}) + \log \pi_{\text{ref}}(\mathbf{x}) + \frac{\lambda - \beta}{\beta} \right) \\ 764 \quad &= \pi_{\text{ref}}(\mathbf{x}) \exp \left(\frac{1}{\beta} R(\mathbf{x}) \right) \exp \left(\frac{\lambda - \beta}{\beta} \right) \end{aligned} \quad (23)$$

768 The term $\exp \left(\frac{\lambda - \beta}{\beta} \right)$ is a constant that does not depend on \mathbf{x} . This constant serves as the normalization factor to ensure that $\int \pi^*(\mathbf{x}) d\mathbf{x} = 1$. Let us denote this normalization constant as $1/Z(\beta)$. Therefore, the optimal distribution is:

$$\pi^*(\mathbf{x}) = \frac{1}{Z(\beta)} \pi_{\text{ref}}(\mathbf{x}) \exp \left(\frac{1}{\beta} R(\mathbf{x}) \right) \quad (24)$$

774 This is equivalent to the proportional relationship given in Equation 8:

$$\pi^*(\mathbf{x}) \propto \pi_{\text{ref}}(\mathbf{x}) \exp \left(\frac{1}{\beta} R(\mathbf{x}) \right) \quad (25)$$

778 This completes the proof.

780 C.2 EQUIVALENCE OF THE DPO OBJECTIVE

782 The Direct Preference Optimization (DPO) framework is derived by re-parameterizing the KL-
783 regularized RL objective in terms of preferences, thereby avoiding the need to explicitly train a
784 reward model. The derivation shows that optimizing the DPO loss is equivalent to optimizing the
785 policy towards the same theoretical distribution π^* derived above.

786 The derivation proceeds as follows:

788 1. **Express Reward in terms of Policies:** We start with the optimal policy solution from the
789 previous section and rearrange it to solve for the reward function $R(\mathbf{x})$:

$$\begin{aligned} 790 \quad \pi^*(\mathbf{x}) &= \frac{1}{Z(\beta)} \pi_{\text{ref}}(\mathbf{x}) \exp \left(\frac{1}{\beta} R(\mathbf{x}) \right) \\ 791 \quad \implies R(\mathbf{x}) &= \beta \log \left(\frac{\pi^*(\mathbf{x})}{\pi_{\text{ref}}(\mathbf{x})} \right) + \beta \log Z(\beta) \end{aligned} \quad (26)$$

795 The term $\beta \log Z(\beta)$ is a constant with respect to \mathbf{x} .

796 2. **Model Human Preferences:** Human preferences are typically collected as pairs $(\mathbf{x}_w, \mathbf{x}_l)$,
797 where \mathbf{x}_w is preferred over \mathbf{x}_l . The Bradley-Terry model maps reward scores to preference
798 probabilities:

$$p(\mathbf{x}_w \succ \mathbf{x}_l) = \sigma(R(\mathbf{x}_w) - R(\mathbf{x}_l)) \quad (27)$$

800 where $\sigma(\cdot)$ is the sigmoid function.

801 3. **Combine Reward and Preference Models:** We substitute the policy-based expression
802 for the reward into the Bradley-Terry model. The constant term $\beta \log Z(\beta)$ cancels out
803 perfectly:

$$\begin{aligned} 805 \quad &R(\mathbf{x}_w) - R(\mathbf{x}_l) \\ 806 \quad &= \left(\beta \log \frac{\pi^*(\mathbf{x}_w)}{\pi_{\text{ref}}(\mathbf{x}_w)} + C \right) - \left(\beta \log \frac{\pi^*(\mathbf{x}_l)}{\pi_{\text{ref}}(\mathbf{x}_l)} + C \right) \\ 807 \quad &= \beta \left(\log \frac{\pi^*(\mathbf{x}_w)}{\pi_{\text{ref}}(\mathbf{x}_w)} - \log \frac{\pi^*(\mathbf{x}_l)}{\pi_{\text{ref}}(\mathbf{x}_l)} \right) \end{aligned} \quad (28)$$

810
811 Thus, the ground-truth preference probability can be expressed entirely in terms of the
812 optimal policy π^* and the reference policy π_{ref} :

813
814
$$p(\mathbf{x}_w \succ \mathbf{x}_l) = \sigma \left(\beta \left(\log \frac{\pi^*(\mathbf{x}_w)}{\pi_{\text{ref}}(\mathbf{x}_w)} - \log \frac{\pi^*(\mathbf{x}_l)}{\pi_{\text{ref}}(\mathbf{x}_l)} \right) \right) \quad (29)$$

815

816 4. **Construct the DPO Loss:** DPO seeks to find a policy π_θ that maximizes the log-likelihood
817 of the observed human preferences. This is equivalent to minimizing the negative log-
818 likelihood loss. By replacing the theoretical optimal policy π^* with our parameterized
819 model policy π_θ , we arrive at the DPO loss function:

820
$$\mathcal{L}_{\text{DPO}} = -\mathbb{E}_{(\mathbf{x}_w, \mathbf{x}_l) \sim \mathcal{D}} (\log p(\mathbf{x}_w \succ \mathbf{x}_l)) \quad (30)$$

821

822 By minimizing this loss, we are directly training the policy π_θ to satisfy the same mathematical
823 relationship that defines the optimal RL policy π^* . Therefore, the policy obtained by successfully
824 optimizing the DPO objective, π_{DPO}^* , converges to the same theoretical distribution as the one
825 found by KL-regularized RL, where the reward function $R(\mathbf{x})$ is implicitly defined by the human
826 preference dataset.

828 C.3 DERIVATION OF VELOCITY-SCORE RELATIONSHIP

829 This section provides a detailed derivation of the relationship between the velocity field $\mathbf{v}(\mathbf{x}, t)$ used
830 in Flow Matching models and the score function $\mathbf{s}(\mathbf{x}, t)$ used in Denoising Diffusion Models, as
831 stated in Equation 2.

832 The unifying perspective relies on a common reference path $(X_t)_{t \in [0, 1]}$ that interpolates between an
833 initial noise variable $X_1 \sim p_1 = \mathcal{N}(0, \mathbf{I})$ and a data sample $X_0 \sim p_{\text{data}}$. This path is defined by
834 linear interpolation:

835
$$X_t = \beta_t X_1 + \alpha_t X_0 \quad (31)$$

836 where α_t and β_t are scalar functions of time, with $\alpha_0 = \beta_1 = 0$ and $\alpha_1 = \beta_0 = 1$.

837 In Denoising Diffusion Models, the model learns to predict the score function $\mathbf{s}(\mathbf{X}_t, t) = \nabla_{\mathbf{X}_t} \log p_t(\mathbf{X}_t)$. For the chosen linear interpolation path where $X_1 \sim \mathcal{N}(0, \mathbf{I})$, it's a known property
838 that the score function is related to the conditional expectation of X_0 and X_1 given X_t . Specifically,
839 the optimal denoised estimate of X_0 , denoted $\hat{X}_0(\mathbf{X}_t, t)$, and the optimal estimate of the noise X_1 ,
840 denoted $\hat{X}_1(\mathbf{X}_t, t)$, can be expressed in terms of X_t and its score:

841
$$\hat{X}_0(\mathbf{X}_t, t) = \mathbb{E}[X_0 | X_t] = \frac{1}{\alpha_t} (\mathbf{X}_t + \beta_t^2 \mathbf{s}(\mathbf{X}_t, t)) \quad (32)$$

842
$$\hat{X}_1(\mathbf{X}_t, t) = \mathbb{E}[X_1 | X_t] = -\beta_t \mathbf{s}(\mathbf{X}_t, t) \quad (33)$$

843 These relationships hold under the assumption that the conditional distribution $p(X_t | X_0)$ is a Gaussian
844 $X_t \sim \mathcal{N}(\alpha_t X_0, \beta_t^2 \mathbf{I})$, which is implied by the path definition with $X_1 \sim \mathcal{N}(0, \mathbf{I})$.

845 For Flow Matching models, the objective is to learn a velocity field $\mathbf{v}(\mathbf{X}_t, t)$ that describes the
846 deterministic trajectory of samples via an ordinary differential equation $d\mathbf{X}_t = \mathbf{v}(\mathbf{X}_t, t)dt$. This
847 velocity field matches the time derivative of the reference flow, $\frac{d}{dt} X_t$. Differentiating Equation 31
848 with respect to time t :

849
$$\mathbf{v}(\mathbf{X}_t, t) = \frac{d}{dt} X_t = \dot{\beta}_t X_1 + \dot{\alpha}_t X_0 \quad (34)$$

850 To express the velocity field in terms of the current state \mathbf{X}_t and the score function $\mathbf{s}(\mathbf{X}_t, t)$, we sub-
851 stitute the expressions for $\hat{X}_0(\mathbf{X}_t, t)$ (Equation 32) and $\hat{X}_1(\mathbf{X}_t, t)$ (Equation 33) into Equation 34:

852
$$\mathbf{v}(\mathbf{X}_t, t) = \dot{\beta}_t (-\beta_t \mathbf{s}(\mathbf{X}_t, t)) + \dot{\alpha}_t \left(\frac{1}{\alpha_t} (\mathbf{X}_t + \beta_t^2 \mathbf{s}(\mathbf{X}_t, t)) \right)$$

853
$$= -\dot{\beta}_t \beta_t \mathbf{s}(\mathbf{X}_t, t) + \frac{\dot{\alpha}_t}{\alpha_t} \mathbf{X}_t + \frac{\dot{\alpha}_t}{\alpha_t} \beta_t^2 \mathbf{s}(\mathbf{X}_t, t)$$

864 Rearranging the terms by grouping \mathbf{X}_t and $\mathbf{s}(\mathbf{X}_t, t)$:

$$\begin{aligned} 866 \quad \mathbf{v}(\mathbf{X}_t, t) &= \left(\frac{\dot{\alpha}_t}{\alpha_t} \right) \mathbf{X}_t + \left(\frac{\dot{\alpha}_t}{\alpha_t} \beta_t^2 - \dot{\beta}_t \beta_t \right) \mathbf{s}(\mathbf{X}_t, t) \\ 867 \\ 868 \quad &= \left(\frac{\dot{\alpha}_t}{\alpha_t} \right) \mathbf{X}_t + \beta_t \left(\frac{\dot{\alpha}_t}{\alpha_t} \beta_t - \dot{\beta}_t \right) \mathbf{s}(\mathbf{X}_t, t) \end{aligned} \quad (35)$$

871 This derivation confirms Equation 2 from the main paper, establishing the precise mathematical
872 connection between the velocity field learned by Flow Matching and the score function predicted by
873 Denoising Diffusion Models under the common linear interpolation path.

875 D DERIVATION OF THE IMPLICIT TIME-DEPENDENT REWARD

877 To formalize this, we first need to establish that for any given generative model policy π_θ (rep-
878 presented by its distribution $p_{\theta,t}$), we can define a corresponding reward function for which π_θ is
879 the optimal policy. This concept is well-established in inverse reinforcement learning for discrete
880 MDPs, such as those used for aligning LLMs Sun et al. (2025); Rafailov et al. (2023). We can ex-
881 tend this framework to diffusion models by considering the generation process as a continuous-time
882 MDP Black et al. (2023); Rafailov et al. (2024).

883 In this diffusion MDP, the state at time t is the noisy sample \mathbf{x}_t , and the policy $\pi(\cdot|\mathbf{x}_t)$ determines
884 the transition to the next state \mathbf{x}_{t-dt} . Recent theoretical work has shown a bijection between re-
885 ward functions and optimal Q-functions (and thus optimal policies) in such MDPs. Specifically,
886 following Rafailov et al. (2024), for a given reference policy π_{ref} and a temperature parameter β , the
887 optimal policy π^* for a reward function $r(s_t, a_t)$ satisfies the relationship:

$$888 \quad \beta \log \frac{\pi^*(a_t|s_t)}{\pi_{\text{ref}}(a_t|s_t)} = r(s_t, a_t) + \Phi(s_{t-dt}) - \Phi(s_t) \quad (36)$$

890 where Φ is a potential function, corresponding to the optimal value function V^* . This means that any
891 policy π_θ can be viewed as the optimal policy for an implicitly defined reward function, equivalent
892 to the log-policy ratio up to a potential-based shaping term.

893 By adapting this principle to the continuous state-space of diffusion models, we can define an in-
894 *stantaneous*, time-dependent reward function $R_t(\mathbf{x}_t)$ directly in terms of the model's probability
895 density. The policy $\pi_\theta(\cdot|\mathbf{x}_t)$ is governed by the underlying score function $\mathbf{s}_\theta(\mathbf{x}_t, t)$, which itself is
896 the gradient of the log-density $\log p_{\theta,t}(\mathbf{x}_t)$. We can therefore define the implicit reward by relating
897 the marginal densities of the RL-aligned model ($p_{\theta,t}$) and the reference model ($p_{\text{ref},t}$):

$$900 \quad R_t(\mathbf{x}_t) \triangleq \beta \log \frac{p_{\theta,t}(\mathbf{x}_t)}{p_{\text{ref},t}(\mathbf{x}_t)} \quad (37)$$

902 Here, $p_{\theta,t}$ is the marginal probability distribution of the noisy image \mathbf{x}_t under the RL-aligned model,
903 and $p_{\text{ref},t}$ is the corresponding distribution for the pre-trained reference model. The parameter β is
904 the same KL-regularization coefficient from the original RL objective (Equation 7). This equation
905 defines the reward that the RL-aligned model π_θ is implicitly optimizing for at every point (\mathbf{x}_t, t) in
906 the generation process, relative to the reference model.

908 E ONE-DIMENSIONAL CASE STUDY OF MODEL CONVERGENCE

910 We further investigate how RLG behaves under different RL algorithms when the RL policy does *not*
911 converge to the ideal reward-reweighted distribution, and why RLG can still improve performance
912 in this realistic regime. To this end, we construct a small-scale one-dimensional case study. Our
913 setting uses a flow-matching model defined on the real line with a pretrained base Gaussian mixture
914 distribution

$$915 \quad p_{\text{base}}(x) \triangleq 0.7 \mathcal{N}(-2.5, 0.25) + 0.3 \mathcal{N}(2.5, 0.49).$$

916 To bias the model toward a specific region, we introduce a reward function that assigns higher reward
917 to samples near $x = 4$; concretely, we use $r(x) = -0.1|x - 4|$ (up to an additive constant), so that
918 points closer to $x = 4$ receive larger reward. We then fine-tune the pretrained flow with either a

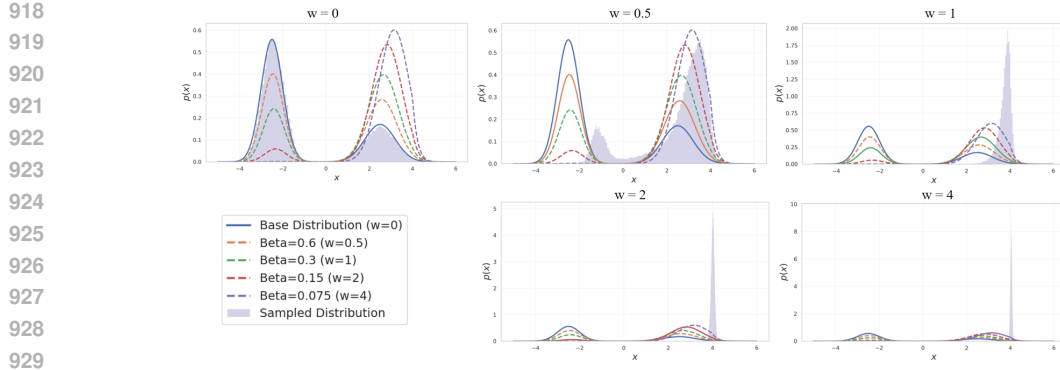


Figure 3: Small-scale demonstration supporting the theoretical justification of RLG. Each subplot shows the sampled distribution under a different RLG weight w , while the curves represent the corresponding theoretically predicted RL-fine-tuned distributions. Here, β denotes the KL regularization coefficient.

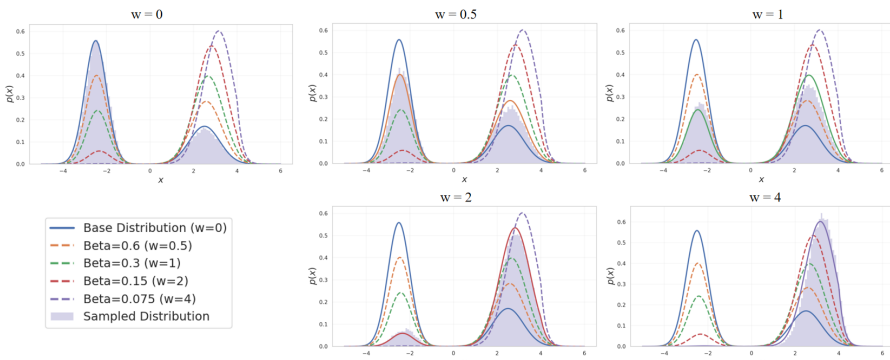


Figure 4: Small-scale demonstration supporting the theoretical justification of RLG. Each subplot shows the sampled distribution under a different RLG weight w , while the curves represent the corresponding theoretically predicted RL-fine-tuned distributions. Here, β denotes the KL regularization coefficient.

vanilla policy-gradient method or the GRPO algorithm, using a KL coefficient $\beta = 0.3$, batch size 64, and learning rate 1×10^{-5} , with the pretrained flow as the reference policy.

Figures 3 and 4 show the sampled distributions under different RLG weights w , together with the corresponding reward-reweighted target $p_{rl}(x) \propto p_{base}(x) \exp(r(x)/\beta)$. For both the policy-gradient and GRPO experts, increasing w from 0.5 to 1, 2, and 4 consistently shifts probability mass toward the high-reward region around $x = 4$: the left-hand mode is gradually suppressed, and the right-hand mode becomes sharper near the reward peak. In the GRPO case, the standalone RL policy already produces a very sharp and imperfect approximation of the target distribution, yet applying RLG on top of this expert still moves the overall sampler closer to the high-reward region. This toy example illustrates that even when the RL policy does not exactly realize the ideal distribution (as is typical for practical algorithms such as GRPO), RLG with a moderate weight w can reliably steer samples toward higher-reward regions and improve alignment over both the base model and the raw RL-fine-tuned model.

F EXPERIMENTAL DETAILS

F.1 GENERATION HYPER-PARAMETERS

This section provides a detailed overview of the parameters and settings used for the text-to-image generation experiments discussed in the main paper.

972 To ensure consistency across our evaluations, several parameters were standardized for all models.
 973 All images were generated at a resolution of 512×512 pixels. Text prompts were processed using
 974 the models' respective text encoders; For the generative process, we uniformly set the number of
 975 sampling steps to 20 for all experiments to maintain a balance between computational cost and
 976 output quality.

977 The Classifier-Free Guidance (CFG) scale, which controls the adherence to the text prompt, was set
 978 to the generally recommended value for each model to ensure optimal baseline performance. The
 979 specific CFG scales used were:
 980

- **Stable Diffusion 1.4:** A CFG scale of 7.5 was used.
- **Stable Diffusion 1.5:** A CFG scale of 7.5 was used.
- **Stable Diffusion inpainting:** A CFG scale of 7.5 was used.
- **Stable Diffusion XL:** A CFG scale of 5.0 was used.
- **Stable Diffusion 3.5:** A CFG scale of 4.5 was used.

981 These CFG scales were held constant across all experiments for a given model, allowing for a direct
 982 assessment of the impact of our RLG guidance scale (w). Other parameters are kept default as
 983 diffusers pipeline.
 984

985 F.2 HUMAN PREFERENCE EVALUATION METRICS DETAILS

986 To quantitatively evaluate the performance of our method, we established automated reward models.
 987 These models are designed to assess different aspects of image quality and text-to-image alignment,
 988 providing a comprehensive evaluation framework.

- **Aesthetic Score:** This metric provides a general assessment of an image's visual appeal. It utilizes a pre-trained CLIP model ('clip-vit-large-patch14') Radford et al. (2021) to extract a feature embedding from the input image. This embedding is then processed by a Multi-Layer Perceptron (MLP) head, loaded with weights provided in Liu et al. (2025b), which regresses the features into a single scalar score, typically on a 1-to-10 scale. The corresponding links are listed in table 6. A higher score indicates a higher predicted aesthetic quality, as judged by human raters in the dataset the MLP was trained on.
- **ImageReward:** Developed by Xu et al. (2023), this is a sophisticated reward model designed to evaluate both the semantic alignment of an image to its text prompt and its overall visual fidelity. Built upon the BLIP-2 architecture Li et al. (2023), it was fine-tuned on a large-scale dataset of human preference feedback, enabling it to serve as a robust, general-purpose proxy for human judgment in text-to-image generation tasks.
- **PickScore:** Introduced by Kirstain et al. (2023), this reward model is specifically trained to predict human preferences based on direct pairwise comparisons. It is derived from the extensive Pick-a-Pic dataset, which contains a vast number of human choices between two images generated from the same prompt. We use the v1 version, which leverages a powerful 'CLIP-ViT-H-14' model Radford et al. (2021). Its strong correlation with human preference makes it particularly relevant for our work.

1016 G GENEval BENCHMARK DETAILS

1017 The **GenEval** benchmark provides an automated, object-focused framework for evaluating the com-
 1018 positional capabilities of text-to-image models Ghosh et al. (2023). Unlike holistic metrics that
 1019 measure overall image quality or text alignment, GenEval offers a fine-grained analysis of a model's
 1020 ability to adhere to specific compositional instructions within a prompt.
 1021

1022 The official test set is comprised of 553 prompts. the prompts are designed to probe several distinct
 1023 aspects of compositional generation:
 1024

- **Single Object:** Tests the model's fundamental ability to render a single specified object.

- **Two Objects:** Assesses the capacity to generate two distinct objects in the same image, testing for co-occurrence.
- **Counting:** Evaluates whether the model can generate a precise number of a given object.
- **Colors:** Measures if an object can be rendered with a specific, designated color.
- **Position:** Tests spatial reasoning by requiring two objects to be placed in a specified relative position (e.g., "a cat to the left of a dog").
- **Attribute Binding:** The most complex task, which requires binding specific attributes (like color) to specific objects (e.g., generating "a red cube and a blue sphere" without swapping attributes).

The evaluation protocol is fully automated, using a sophisticated object detection model to parse the generated images. For our experiments, we adhered to the official methodology, which employs a **Mask2Former** Cheng et al. (2022) model with a Swin-S transformer backbone Liu et al. (2021). This detector identifies objects and verifies their properties and spatial arrangements as dictated by the input prompt.

H IMAGE COMPRESSIBILITY EXPERIMENTAL DETAILS

This section provides a detailed description of the experimental setup for the image compressibility task.

Models and Task Definition. The goal of this experiment was to verify that Reinforcement Learning Guidance (RLG) can effectively control a low-level, non-semantic property of generated images: their compressibility. We used the standard Stable Diffusion v1.4 model as our base reference (\mathbf{v}_{ref}). For the aligned models (\mathbf{v}_θ), we utilized two sets of weights from the official DDPO implementation Black et al. (2023):

- **Low Compressibility Model:** We use ddpo-compressibility. This model was fine-tuned to generate images that are less compressible, resulting in larger file sizes when saved in JPEG format. This typically corresponds to images with higher texture detail and complexity.
- **High Compressibility Model:** We use ddpo-incompressibility. This model was fine-tuned to prefer images that are more compressible, resulting in smaller JPEG file sizes. This often corresponds to images with smoother regions and less high-frequency detail.

Dataset and Prompts. Following the DDPO study Black et al. (2023), our evaluation prompts were based on animal classes from the ImageNet dataset. We used 45 distinct animal classes. For each class, we generated 4 images, resulting in a total of 180 images per RLG scale setting. The prompt template used was: "{class_name}".

The 45 animal classes used are: ant, bat, bear, bee, beetle, bird, butterfly, camel, cat, chicken, cow, deer, dog, dolphin, duck, fish, fly, fox, frog, goat, goose, gorilla, hedgehog, horse, kangaroo, lion, lizard, llama, monkey, mouse, pig, rabbit, raccoon, rat, shark, sheep, snake, spider, squirrel, tiger, turkey, turtle, whale, wolf, and zebra.

Evaluation Metric. We evaluated performance using the **Compression Ratio**. For a given prompt, let \mathbf{x}_{base} be the image generated by the base SD1.4 model, and let $\mathbf{x}_{\text{RLG}}(w)$ be the image generated using RLG with a guidance scale of w . Let $S_{\text{jpeg}}(\cdot)$ denote the file size of an image after being compressed and saved in JPEG format. The Compression Ratio is defined as:

$$\text{Compression Ratio}(w) = \frac{S_{\text{jpeg}}(\mathbf{x}_{\text{RLG}}(w))}{S_{\text{jpeg}}(\mathbf{x}_{\text{base}})}$$

The final score reported in Table 5 is the mean of this ratio, averaged across all 180 generated images for each guidance scale. A ratio of 1.0 indicates no change in compressibility compared to the base model.

1080 I IMAGE INPAINTING EXPERIMENTAL DETAILS
10811082 This section provides a comprehensive overview of the experimental setup, models, and evaluation
1083 protocol used for the image inpainting task discussed in the main paper. Our methodology closely
1084 follows that of the PrefPaint Bui et al. (2025) study to ensure a fair and direct comparison.
10851086 I.1 MODELS AND TASK DEFINITION
10871088 The experiment focuses on conditional image generation for image inpainting, the task of filling in
1089 masked (missing) regions of an image in a semantically and visually plausible manner.
1090

- **Base Model (v_{ref}):** We use the standard Stable Diffusion inpainting model as our baseline. This model, accessible on diffusers as `runwayml/stable-diffusion-inpainting`, is widely used and serves as the un-aligned reference point for our experiments.
- **RL-Finetuned Model (v_θ):** For the human-preference-aligned expert model, we employ **PrefPaint** Bui et al. (2025). This model is a direct descendant of the base model, which has been further fine-tuned using reinforcement learning. The training process for PrefPaint leveraged a large-scale dataset of over 51,000 human preference judgments on inpainted images, making it an expert policy specialized in generating completions that align with human aesthetic and contextual expectations.

1101 I.2 EVALUATION DATASET AND PROTOCOL
11021103 All quantitative results were generated using the dataset provided by the authors of PrefPaint Bui
1104 et al. (2025). The test set was constructed using the following procedure:
1105

1. **Image Sourcing:** A diverse set of high-resolution images was initially sourced from established datasets such as ADE20K and ImageNet. All images were resized to a standard 512×512 pixel resolution.

2. **Mask Generation:** To simulate realistic inpainting and outpainting scenarios, two distinct masking strategies were employed to create the incomplete images:

- **Warping Holes (for Inpainting):** This method creates complex, non-rectangular masks inside the image. It simulates the disocclusion that occurs from a slight change in camera viewpoint. A depth map is first estimated for the source image, and then a new virtual camera view is generated with small shifts. The newly visible (disoccluded) regions form the mask that the model must fill. This tests the model's ability to reason about 3D geometry and handle irregular shapes.

- **Boundary Masks (for Outpainting):** This strategy tests the model's ability to extend a scene beyond its original borders. Masks are created at the edges of the image using two different cropping techniques:

- *Square Cropping:* A central square region, covering 75% to 85% of the image area, is preserved, masking the outer frame.

- *Rectangular Cropping:* The full height of the image is preserved, while a central vertical slice, comprising 60% to 65% of the original width, is kept, masking the left and right sides.

1125 I.3 EVALUATION METRICS
11261127 The quality of the generated inpainted images was assessed using the following two automated
1128 metrics:
1129

- **Preference Reward:** We use the specialized reward model developed and released as part of the PrefPaint study Bui et al. (2025). This model was trained on their custom dataset of nearly 51,000 human preference annotations. Unlike a general-purpose aesthetics model, it is specifically tailored to judge the quality of image inpainting, considering factors like structural rationality, local texture coherence, and overall aesthetic feeling. The reward

1134 scores reported in our table are the normalized values from this model, averaged over the
 1135 official test set, as done in the original paper.
 1136

1137 J PERSONALIZED IMAGE GENERATION EXPERIMENTAL DETAILS

1139 This appendix provides a detailed overview of the experimental setup for evaluating Reinforcement
 1140 Learning Guidance (RLG) on the task of personalized image generation, as presented in the main
 1141 paper.
 1142

1143 J.1 TASK AND MODEL BACKGROUND

1145 **Task Definition.** Personalized image generation aims to synthesize novel images of a specific
 1146 subject provided through one or more reference images. The model is given a reference image
 1147 containing the subject (e.g., a specific pet dog) and a text prompt (e.g., "a photo of [V] sleeping on
 1148 a couch," where [V] is a placeholder for the subject). The primary goal is to generate an image that
 1149 not only matches the prompt's description but also maintains high fidelity to the unique appearance
 1150 and characteristics of the subject in the reference image.
 1151

1152 **Model Selection.** Our experiment is designed to test if RLG can amplify the effects of a
 1153 fine-grained, RL-based alignment process. We therefore select models based on the work of
 1154 PatchDPO Huang et al. (2025).

- 1155 • **Base Model (v_{ref}):** We use the publicly available, pre-trained **IP-Adapter-Plus** Ye et al.
 1156 (2023) model built on SDXL Podell et al. (2023). IP-Adapter is a powerful method for
 1157 subject-driven generation that injects image features into the cross-attention layers of a
 1158 diffusion model. We use it as our baseline because it represents a strong, general-purpose
 1159 personalization model before any preference-based fine-tuning.
 1160
- 1161 • **RL-aligned Model (v_{θ}):** We use the model fine-tuned from IP-Adapter-Plus using the
 1162 **PatchDPO** algorithm. PatchDPO is a form of preference optimization that operates at a
 1163 sub-image or "patch" level. During its training, generated images are compared against the
 1164 reference image. Patches from the generated image that are consistent with the reference
 1165 subject receive a positive reward, while inconsistent patches are penalized. This process,
 1166 analogous to reinforcement learning with fine-grained rewards, tunes the model to be highly
 1167 specialized in preserving subject fidelity.

1168 J.2 BENCHMARK AND EVALUATION METRICS

1169 **Benchmark Dataset.** All evaluations are conducted on **DreamBench** Ruiz et al. (2023), the stan-
 1170 dard benchmark for personalized image generation. DreamBench consists of 30 unique subjects,
 1171 each with a set of reference images and 80 corresponding text prompts. This benchmark is designed
 1172 to test a model's ability to generate the subject in various contexts, poses, and interactions.
 1173

1174 **Evaluation Metrics.** To quantitatively measure the fidelity of the generated images to the refer-
 1175 ence subject, we employ two standard, complementary metrics. For each prompt in DreamBench,
 1176 we generate an image and compare it to the ground-truth reference images of the subject.
 1177

- 1178 • **CLIP-I (Image Similarity):** This metric, introduced by the DreamBooth authors, mea-
 1179 sures the semantic similarity between the generated and reference images. It works by
 1180 encoding both images into high-dimensional feature vectors using a pre-trained CLIP ViT-
 1181 L/14 image encoder. The final score is the average cosine similarity between the embedding
 1182 of the generated image and the embeddings of the reference images. A higher CLIP-I score
 1183 indicates that the generated image is semantically and stylistically closer to the reference
 1184 subject from the perspective of the CLIP model.
 1185
- 1186 • **DINO (Structural Similarity):** This metric uses features extracted from a self-supervised
 1187 ViT-S/16 DINO Caron et al. (2021) model. DINO is trained without labels and learns to
 1188 capture rich information about object structure, texture, and shape. The metric is calculated
 1189 as the average cosine similarity between the DINO features of the generated and reference

1188 images. It is particularly effective at measuring the preservation of fine-grained details and
 1189 the structural integrity of the subject, making it an excellent indicator of subject fidelity.
 1190

1191

1192 K DETAILED HUMAN PREFERENCE ALIGNMENT RESULTS

1193

1194 This section provides the complete quantitative results for the human preference alignment experiments,
 1195 complementing the summary presented in Table 1 of the main paper. For each model, we
 1196 present two tables: one detailing the absolute mean scores for Aesthetic Score, ImageReward, and
 1197 PickScore across various RLG guidance scales (w_{RL}), and another showing the pairwise win rates
 1198 against the base model ($w_{RL} = 0.0$) and the standard RL-finetuned model ($w_{RL} = 1.0$).
 1199

1200

1201 Table 7: Mean scores for the **SD3.5-M** model series on human preference metrics across various
 1202 RLG scales (w_{RL}). The scale $w_{RL} = 0.0$ corresponds to the original **SD3.5-M** base model, while
 1203 $w_{RL} = 1.0$ represents the model after GRPO finetuning, named **SD3.5M-FlowGRPO-PickScore**.

1204

w_{RL}	Aesthetic Score (\uparrow)	ImageReward (\uparrow)	PickScore (\uparrow)
0.0	5.97	0.99	21.75
1.0	6.45	1.40	23.29
1.2	6.48	1.41	23.36
1.4	6.54	1.40	23.48
1.6	6.57	1.40	23.53
1.8	6.60	1.41	23.56
2.0	6.62	1.40	23.57
2.2	6.64	1.39	23.58
2.4	6.66	1.39	23.58
2.6	6.68	1.37	23.59
2.8	6.68	1.36	23.56

1216

1217

1218

1219 Table 8: Win rates (%) for **SD3.5-M** model series at various RLG scales (w_{RL}) compared against
 1220 the base ($w_{RL} = 0.0$) and GRPO ($w_{RL} = 1.0$) models.

1221

w_{RL}	Win Rate vs. Base ($w_{RL} = 0.0$)			Win Rate vs. GRPO ($w_{RL} = 1.0$)		
	Aesthetic	ImageReward	PickScore	Aesthetic	ImageReward	PickScore
1.0	88.67	82.71	97.61	-	-	-
1.2	89.60	83.59	98.14	57.96	53.42	60.25
1.4	91.31	82.71	97.80	69.29	54.44	74.95
1.8	92.19	80.76	97.71	75.24	54.25	76.27
2.2	92.72	78.91	97.07	77.39	53.56	73.68
2.4	92.87	77.54	96.78	79.10	51.66	72.80

1230

1231

1232

1233 Table 9: Mean scores for **SDXL-base** model series on human preference metrics at various RLG
 1234 scales (w_{RL}). The scale $w_{RL} = 0.0$ corresponds to the original **SDXL-base** base model, while
 1235 $w_{RL} = 1.0$ represents the model after SPO finetuning, named **SPO-SDXL-4k-p.10ep**.

1236

w_{RL}	Aesthetic Score (\uparrow)	ImageReward (\uparrow)	PickScore (\uparrow)
0.0	6.10	0.72	21.66
1.0	6.42	1.12	22.69
1.2	6.45	1.13	22.71
1.4	6.48	1.14	22.71

1241

w_{RL}	Win Rate vs. Base ($w_{RL} = 0.0$)			Win Rate vs. SPO ($w_{RL} = 1.0$)		
	Aesthetic	ImageReward	PickScore	Aesthetic	ImageReward	PickScore
1.0	82.13	81.98	92.38	-	-	-
1.2	83.06	81.98	92.19	59.81	54.10	54.64
1.4	83.64	81.20	91.46	62.99	54.15	54.35

Table 10: Win rates (%) for **SDXL-base** model series at various RLG scales (w_{RL}) compared against the base ($w_{RL} = 0.0$) and SPO ($w_{RL} = 1.0$) models.

Table 11: Mean scores for **SD1.5** model series on human preference metrics at various RLG scales (w_{RL}). The scale $w_{RL} = 0.0$ corresponds to the original **SD1.5** base model, while $w_{RL} = 1.0$ represents the model after DPO finetuning, named **dpo-sd1.5-text2image-v1**.

w_{RL}	Aesthetic Score (\uparrow)	ImageReward (\uparrow)	PickScore (\uparrow)
0.0 (Base)	5.51	-0.02	20.03
1.0 (DPO)	5.61	0.20	20.39
1.2	5.62	0.22	20.42
1.4	5.62	0.25	20.46
1.6	5.64	0.26	20.51
1.8	5.63	0.29	20.51
2.0	5.64	0.31	20.54
2.2	5.64	0.31	20.55
2.4	5.64	0.32	20.56

Table 12: Win rates (%) for **SD1.5** at various RLG scales (w_{RL}) compared against the base ($w_{RL} = 0.0$) and standard DPO ($w_{RL} = 1.0$) models.

w_{RL}	Win Rate vs. Base ($w_{RL} = 0.0$)			Win Rate vs. DPO ($w_{RL} = 1.0$)		
	Aesthetic	ImageReward	PickScore	Aesthetic	ImageReward	PickScore
1.0	61.52	63.33	72.66	-	-	-
1.4	64.11	63.82	75.34	53.56	53.47	57.86
1.8	63.92	66.36	76.27	55.71	56.69	61.43
2.2	64.55	66.46	76.22	56.40	56.64	61.72
2.4	64.21	66.31	76.61	56.25	57.08	61.23

L SELECTED IMAGE GENERATED

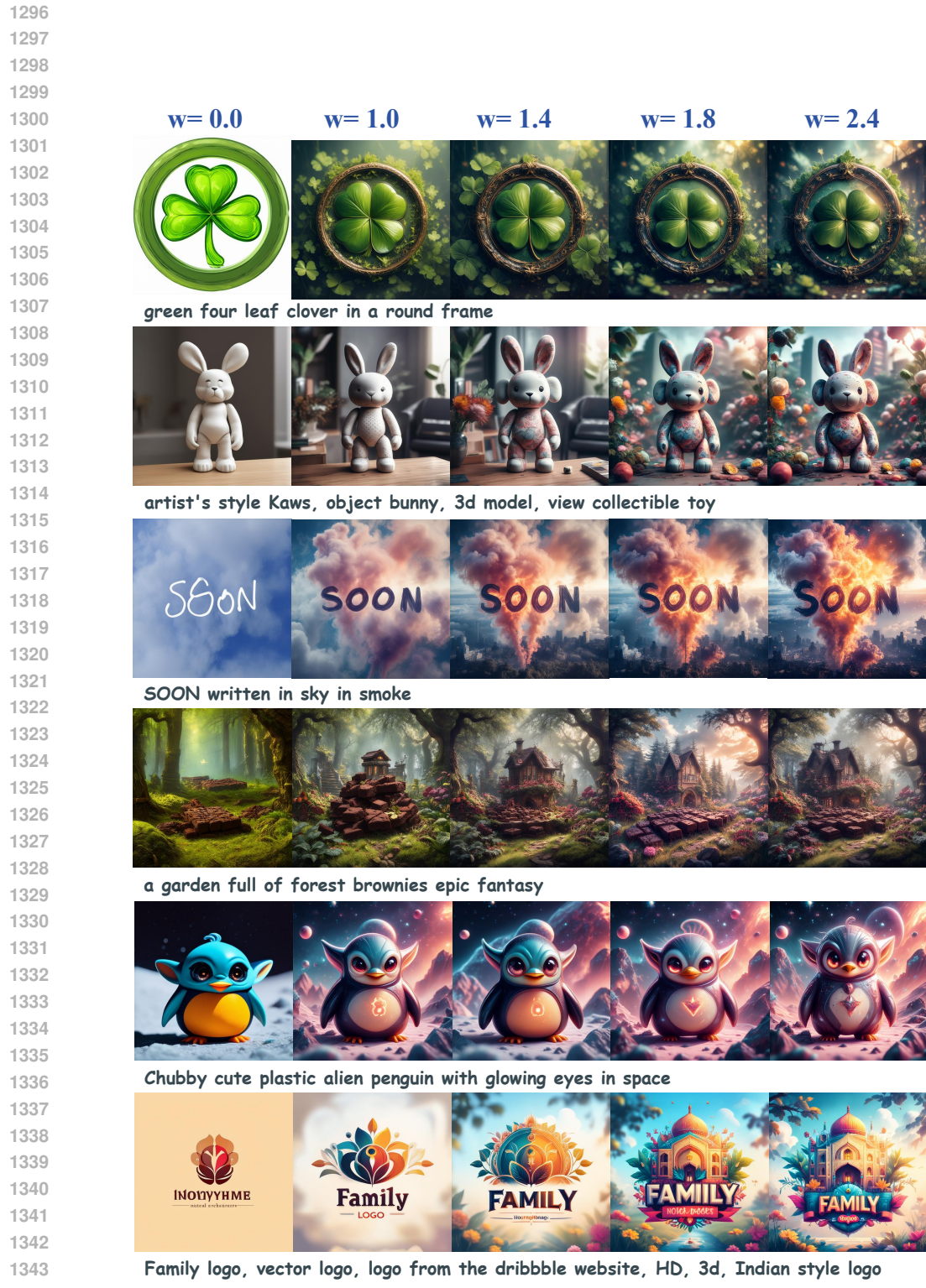
L.1 AESTHETIC IMAGES GENERATED

L.2 OCR IMAGES GENERATED

L.3 COMPRESSIBILITY AND INCOMPRESSIBILITY IMAGES GENERATED

L.4 GENEVAL IMAGES GENERATED

L.5 INPAINTING IMAGES GENERATED



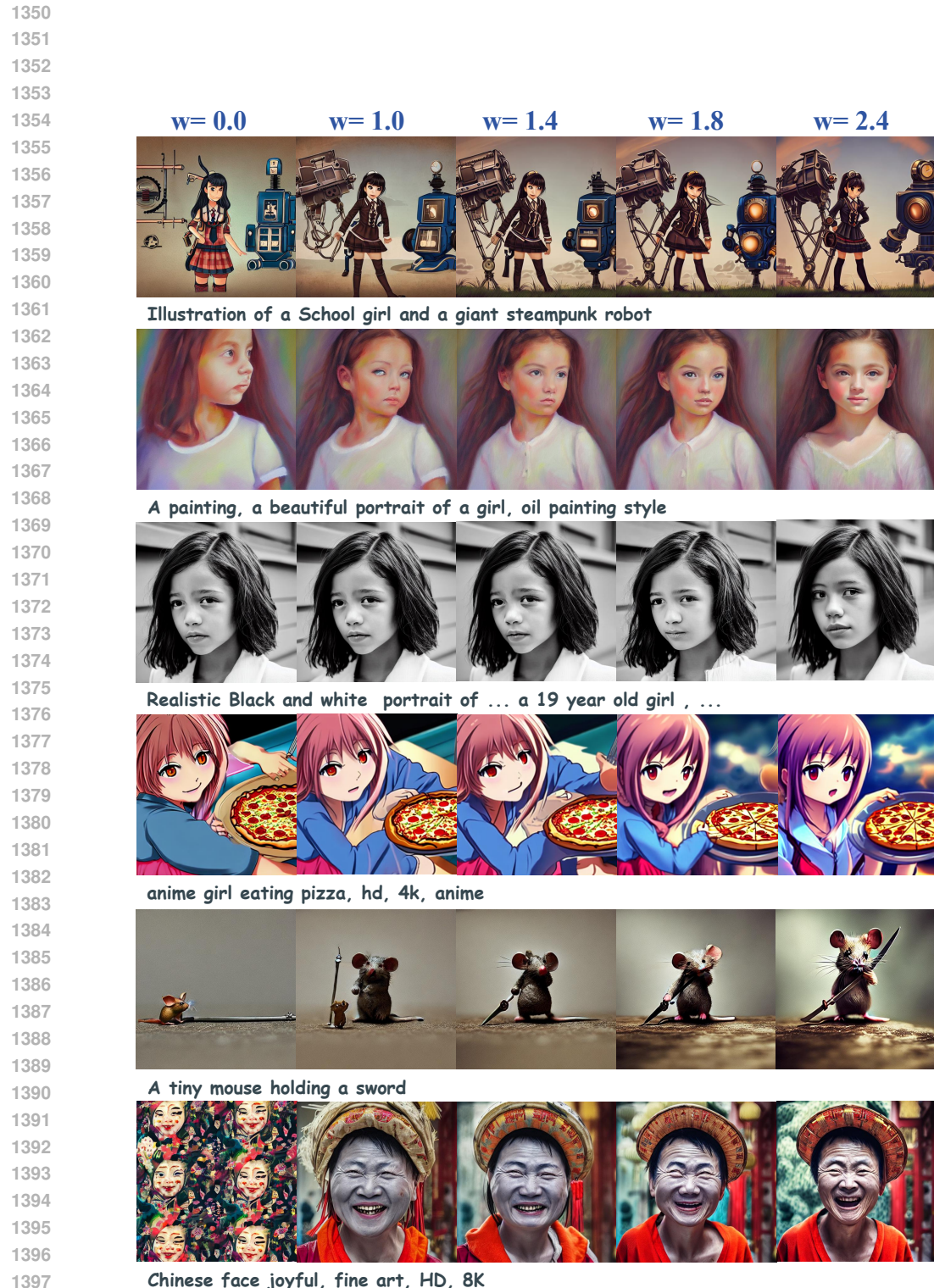


Figure 6: Selected qualitative results for the human preference task. Images are generated from SD1.5 trained with DPO, with different RLG scales.

1404

1405

1406

1407

w = 0.0



w = 1.0



w = 1.2



w = 1.4



1409
1410
1411
1412
1413
1414
1415
1416
mechanical giraffe, electronics, ... led instead of eyes



1417
1418
1419
1420
1421
1422
1423
1424
1425
Marilyn Manson sticking tongue out wearing sunglasses holding a sign that says Famousa



1426
1427
1428
1429
1430
1431
1432
1433
1434
Egirl with orange hair, gorgeous, high-quality, beautiful



1435
1436
1437
1438
1439
1440
1441
1442
1443
The background of the cover should be the campus scenery of the primary school ...



1444
1445
1446
1447
1448
1449
1450
1451
1452
a minimalistic style logo for a game ... studies market and information design

1453
1454
Figure 7: Selected qualitative results for the human preference task. Images are generated from SDXL trained with SPO, with different RLG scales.

1455

1456

1457

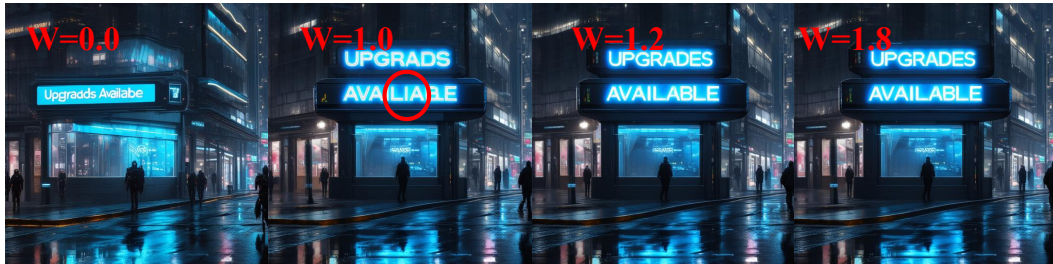
1458
1459
1460
1461
1462
1463
1464
1465
1466
1467
1468
1469
1470
1471
1472
1473
1474
1475



" Bandit Who Stole the D "



" Sample XZ42 "



" Upgrades Available "

Figure 8: Selected qualitative results for the visual text rendering task. As can be seen, the standard RL-finetuned model ($w = 1.0$) still produces some errors in the generated text. By applying RLG with a higher guidance scale ($w > 1.0$), the model correctly renders the specified text without any loss in image quality. This illustrates how RLG effectively enhances the model's ability to adhere to precise instructions.

1504
1505
1506
1507
1508
1509
1510
1511

1512

1513

1514

1515

1516

1517

1518

1519

1520

1521

1522

1523

1524

1525

1526

1527

1528

1529

1530

1531

1532

1533

1534

1535

1536

1537

1538

1539

1540

1541

1542

1543

1544

1545

1546

1547

1548

1549

1550

1551

1552

1553

1554

1555

1556

1557

1558

1559

1560

1561

1562

1563

1564

1565



Figure 9: Selected qualitative results for the image compressibility task.

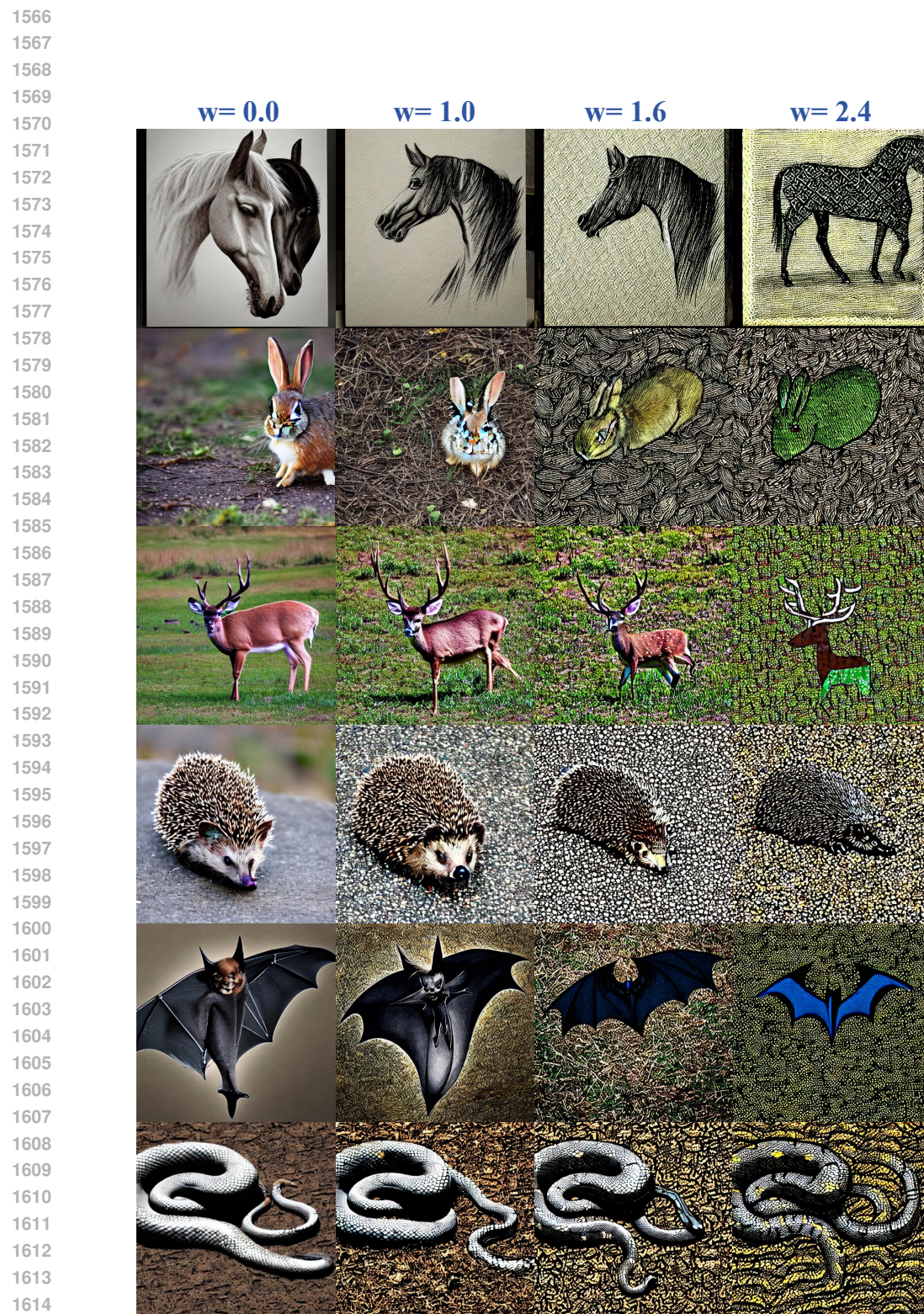


Figure 10: Selected qualitative results for the image compressibility task.

1620

1621

1622

1623

w = 0.0



w = 1.0



w = 1.2



w = 1.8



a photo of a blue pizza and a yellow baseball glove



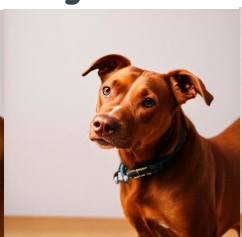
a photo of a yellow bicycle and a red motorcycle



a photo of a white orange



a photo of a red giraffe



a photo of a red dog

Figure 11: Selected qualitative results for the compositional image generation task.

1668

1669

1670

1671

1672

1673

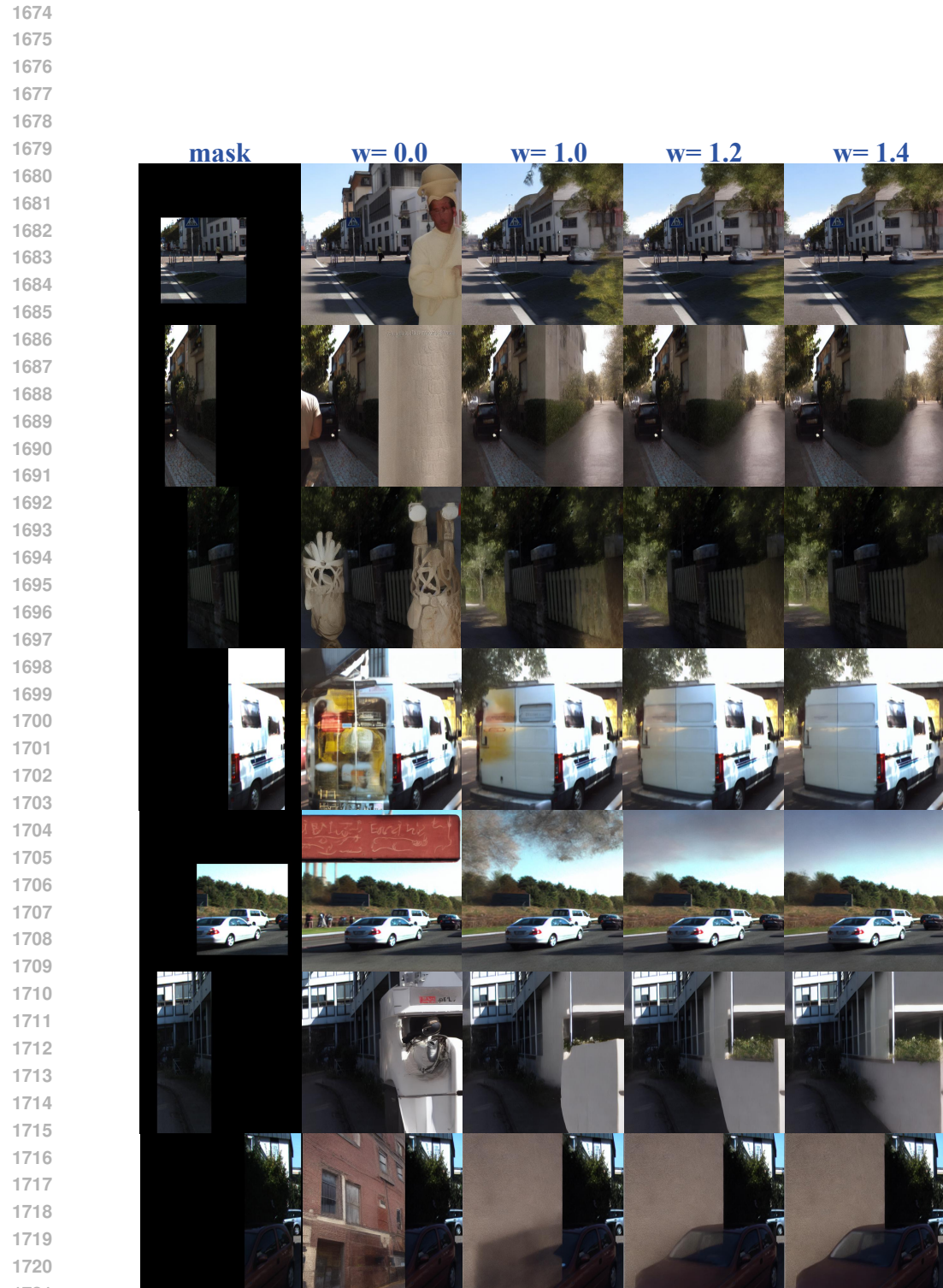


Figure 12: Selected qualitative results for the image inpainting task.